nature communications

Article

https://doi.org/10.1038/s41467-025-59070-0

An organ-wide spatiotemporal transcriptomic and cellular atlas of the regenerating zebrafish heart

Received: 12 June 2024

Accepted: 10 April 2025

Published online: 19 April 2025

Check for updates

Lei Li[1,2,16], Meina Lu[3,4,16], Lidong Guo[1,5,16], Xuejiao Zhang[3,4,16], Qun Liu[1,6,16], Meiling Zhang[3,4,16], Junying Gao[3,4], Mengyang Xu[1,2], Yijian Lu[3,4], Fang Zhang[3,7], Yao Li[1], Ruihua Zhang[1], Xiawei Liu[1], Shanshan Pan[1], Xianghui Zhang[1], Zhen Li[1], Yadong Chen[1], Xiaoshan Su[1,6], Nannan Zhang[1], Wenjie Guo[1], Tao Yang[8], Jing Chen[8], Yating Qin[1,6], Zhe Zhang[9], Wei Cui[1], Lindong Yu[3,4], Ying Gu[2,10], Huanming Yang[2,10], Xun Xu[2,10], Jianxun Wang[11], Caroline E. Burns[12,13], C. Geoffrey Burns[12,13], Kai Han[1,6] ✉, Long Zhao[3,4] ✉, Guangyi Fan[1,2,14,15] ✉ & Ying Su[3,7] ✉

Adult zebrafish robustly regenerate injured hearts through a complex orchestration of molecular and cellular activities. However, this remarkable process, which is largely non-existent in humans, remains incompletely understood. Here, we utilize integrated spatial transcriptomics (Stereo-seq) and single-cell RNA-sequencing (scRNA-seq) to generate a spatially-resolved molecular and cellular atlas of regenerating zebrafish heart across eight stages. We characterize the cascade of cardiomyocyte cell states responsible for producing regenerated myocardium and explore a potential role for *tpm4a* in cardiomyocyte re-differentiation. Moreover, we uncover the activation of *ifrd1* and *atp6ap2* genes as a unique feature of regenerative hearts. Lastly, we reconstruct a 4D "virtual regenerating heart" comprising 569,896 cells/spots derived from 36 scRNA-seq libraries and 224 Stereo-seq slices. Our comprehensive atlas serves as a valuable resource to the cardiovascular and regeneration scientific communities and their ongoing efforts to understand the molecular and cellular mechanisms underlying vertebrate heart regeneration.

Cardiovascular disease (CVD) is the leading cause of morbidity and mortality worldwide[1,2]. After myocardial infarction (MI), the human heart replaces infarcted muscle with noncontractile scar tissue because cardiomyocytes in the adult heart lack the proliferative capabilities required for meaningful regeneration[3,4]. Not surprisingly, the scar tissue disrupts the structure and function of the heart, which increases susceptibility to heart failure. The absence of cardiac regeneration is an almost universal feature of adult mammals[5,6]. By contrast, neonates of many mammals can successfully regenerate their hearts after mechanical or ischemic injury for a short time after birth[7–12]. This remarkable regenerative capacity is also observed in adults of many fish and amphibian species, including zebrafish[13–15]. Although more than twenty species have been investigated for their cardiac regenerative potential[16], the underlying mechanisms unique and common to regenerative hearts remain incompletely defined. Identifying those mechanisms will be aided by the generation of highly comprehensive atlases capturing the molecular and cellular events in 3D space and time that follow cardiac injury in both non-regenerative and regenerative species, something that does not exist for virtually all species, including the highly regenerative zebrafish.

A full list of affiliations appears at the end of the paper. ✉e-mail: hankai@genomics.cn; zhaolong@ouc.edu.cn; fanguangyi@genomics.cn; suying@ouc.edu.cn

The zebrafish heart's response to amputation injury commences with clotting and immune responses that seal the wound and clear cellular debris, respectively[17–20]. Additional early responses to injury include transient organ-wide activation of the endocardium and epicardium[21,22], albeit with incompletely understood biological significance[23], and deposition of new extracellular matrix at the injury site[24,25]. To compensate for the loss of cardiomyocytes (CMs), spared CMs along the border zone undergo dedifferentiation and proliferation[26,27], giving rise to new heart muscle along a vascular scaffold[28,29]. As regeneration progresses, the fibrin-rich blood clot is gradually dissolved and replaced by new CMs[30]. Ultimately, the anatomical structure, tissue composition, and function of the injured heart are fully restored. Nevertheless, the precise order of molecular and cellular events that define successful heart regeneration remains incompletely characterized. Recent single-cell studies have examined the molecular profiles of several cell types during zebrafish heart regeneration, including proliferating CMs[31], activated fibroblasts[32], and other non-CM cell subpopulations[33,34]. However, significant gaps in our knowledge remain. In particular, we lack a comprehensive appreciation of the molecular and cellular events, including their spatiotemporal dynamics globally across the organ throughout the entire regeneration window.

Recently, several spatial transcriptomics platforms have emerged for characterizing gene expression patterns in multiple dimensions[35–42]. Particularly, spatial technology tomo-seq was applied to zebrafish heart regeneration based on the cryoinjury model[43]. In this study, we implemented a combinatorial strategy, utilizing the advantages of scRNA-seq and Stereo-seq techniques to generate a high-resolution, organ-wide molecular and cellular map of the regenerating zebrafish heart. We systematically characterized the major lineages and dynamic cell subtypes at multiple time points, including several immediately following injury. Through comparative analysis of regenerative and non-regenerative hearts, we identified several key factors common to regenerative hearts. Collectively, we anticipate that this resource will be highly valuable to investigators studying regeneration of the heart or other organs in multiple species.

Results

Generation of a spatiotemporal transcriptomic and cellular atlas of the regenerating zebrafish heart

Adult zebrafish hearts robustly regenerate amputated or damaged tissue, with the time to completion depending on the injury model[44]. Regeneration following ventricular apex amputation is largely completed by 30 days post-amputation (dpa)[15]. To systematically characterize organ-wide spatiotemporal patterns of gene expression that reflect dynamic cellular responses over the entire regeneration window, we performed spatial transcriptomics and scRNA-seq separately on whole zebrafish hearts at 8 sequential stages, including pre-injury (i.e., uninjured), 6 hours post-amputation (hpa), 12 hpa, 1 dpa, 3 dpa, 7 dpa, 14 dpa, and 28 dpa (Fig. 1a). For the spatial transcriptomics, we collected three sagittal sections from the centers of six hearts per stage ($n = 144$ total sections) and performed Stereo-seq. Based on inclusion criteria, we selected 105 sections containing 159,293 total spots for analysis (Fig. 1a, Supplementary Fig. 1, Supplementary Data 1). Each spot was about 962 μm^2, encompassing approximately 3–8 cells. Hierarchical clustering uncovered 20 unique spot identities that were manually annotated as major cell-type "domains" based on well-established cell type marker genes (Supplementary Fig. 2a, b and Supplementary Data 2). In many cases, annotations contained information about anatomic location or represented cell states and types. Included in the 20 spot annotated domains were 5 border zone (BZ) domains with ventricular myocardium enriched (domain 1–5), which each contained a higher proportion of different states of cardiomyocytes along with specific endocardial cells (domain 1-5), immune cells (domain 1–2) and fibroblasts (domain 3–4) upon injury; 2 remote zone (RZ) domains with ventricular cardiomyocytes and endocardial cells enriched (domain 6-7); a ventricular compact myocardium enriched domain containing cardiomyocytes, endocardial cells, fibroblasts or epicardial cells (domain 8); an atrial myocardium enriched domain containing a higher proportion of atrial cardiomyocytes and endocardial cells (domain 9); a myocardium enriched domain (domain 10) found in both atrium (A) and ventricle (V); immune cells enriched domain, which showed a larger proportion of macrophages, neutrophils and T cells (domain 11); specific injury-related fibroblasts enriched domain (domain 12); specific immune cells, fibroblasts and endocardial cells enriched domain upon injury (domain 13); the epicardial cells enriched domain 14; the smooth muscle cells enriched domain 15; valve domain 16; three domains enriched with red blood cells (domain 17–19) and the domain 20 containing unknown cells (Fig. 1b and Supplementary Fig. 2a, b). The annotations were mapped to the individual spots to delineate the organ-wide spatial distributions for all 20 subtypes across the eight sequential time points (Fig. 1b, Supplementary Figs. 1, 2a).

We also performed scRNA-seq on 6 replicates from uninjured hearts and 3 replicates per post-injury time point ($n = 27$ total), with an average of 7656 cells per replicate, encompassing 206,719 cells total (Fig. 1a, c; Supplementary Fig. 2c and Supplementary Data 1). We identified and manually annotated 25 cell subtypes across 11 main cell lineages (Fig. 1c, Supplementary Fig. 2c, d, and Supplementary Data 2). In contrast to the domains identified by Stereo-seq, which were usually a mixture of multiple cell types, the clusters identified by scRNA-seq typically contained only a single population of cells with the same characteristics (Supplementary Fig. 2b, d). Differences in the populations identified likely reflect the high resolution and sensitivity of scRNA-seq, which was uniquely capable of detecting sparser cell types such as immune cells (neutrophils and T cells), as well as specific subpopulations of fibroblasts, endocardial cells, and endothelial cells. By contrast, the Stereo-seq identified more myocardium-enriched clusters (Supplementary Data 3), likely stemming from the inefficient recovery of cardiomyocytes for scRNA-seq due to their large cell size and elongated shape.

We further applied the cell type decomposition of the annotated cell types derived from scRNA-seq in each major cell-type domain (Fig. 1d). Based on cell-type deconvolution and systematic correlation analysis (Fig. 1d and Supplementary Fig. 3a), cell types identified by scRNA-seq match well with the major cell-type domains detected by Stereo-seq, such as ventricular specific cardiomyocytes, atrial specific cardiomyocytes, bulbus arteriosus (BA) specific smooth muscle cells, valves and epicardium (Fig. 1d and Supplementary Fig. 3a, b). Moreover, the scRNA-seq cell type clusters identified in our data were well correlated with the previous study[32] (Supplementary Fig. 3c). Ultimately, the complementary nature of the approaches ensured that we achieved a highly comprehensive catalog of cell populations from 132 data points containing transcriptomic information drawn from 366,012 spots or cells.

As validation of the experimental approach, our atlas captured several previously documented cellular responses during zebrafish heart regeneration, including endocardial activation, inflammation, epicardial activation, ECM deposition, CM proliferation, and coronary artery revascularization[45]. Specifically, at 6 hpa and 12 hpa, we observed the transient activation of endocardial cells [i.e., Endocardium (activ.)], defined by organ-wide endocardial upregulation of *aldh1a2* (Fig. 1c, Supplementary Fig. 3d, and Supplementary Data 3)[21,22]. Moreover, we documented an early inflammatory response[34], as evidenced by the appearance of proliferating *pcna*$^+$ *grn1*$^+$ macrophages [i.e., Macrophages (prolif.)] at 12 hpa, later peaking in abundance at 1 dpa (Fig. 1c, Supplementary Fig. 3d, and Supplementary Data 3). On 3 dpa, we observed an increase in the percentage of epicardial cells, together with up-regulation of *aldh1a2* in this mesothelial population (Fig. 1c, Supplementary Fig. 3d, and Supplementary Data 3), indicative

https://doi.org/10.1038/s41467-025-59070-0

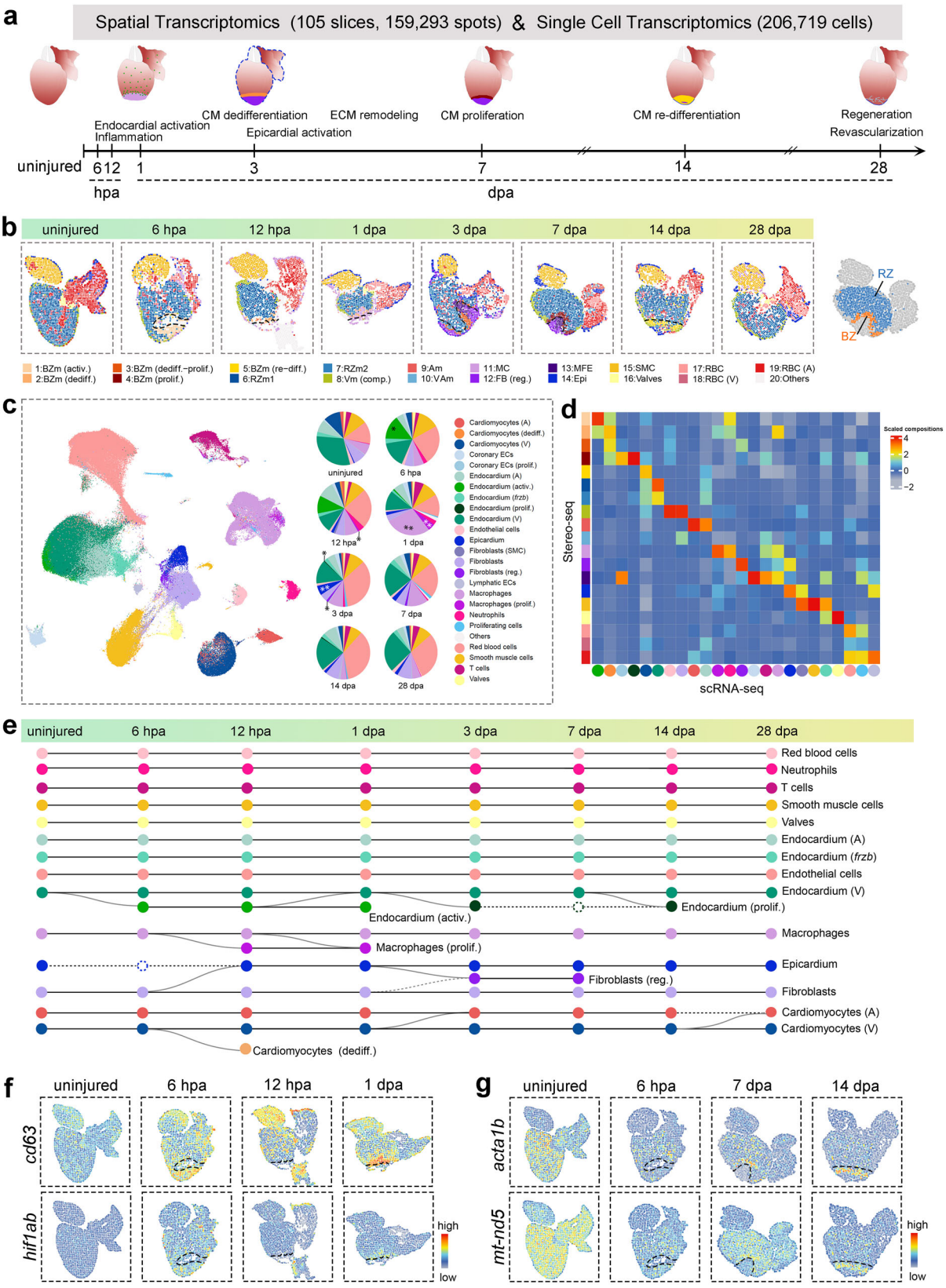

of epicardial activation[21,22]. At 3 and 7 dpa, we detected the presence of *col12a1a*$^{+}$ pro-regenerative fibroblasts [i.e., Fibroblasts (reg.)] in the wound, indicative of ECM deposition (Fig. 1c, Supplementary Fig. 3d and Supplementary Data 3)[32,46,47]. Prior studies have demonstrated that pre-existing CMs along the wound edge undergo dedifferentiation and proliferation, the latter peaking at 7 dpa[15,27,48]. In agreement, we identified a substantial subpopulation of BZ cardiomyocyte-related domains, and detected the expression of *nkx2.5*, *mustn1b*, *hand2* and glycolysis genes *pkma* along the wound edge at 7 dpa (Fig. 1b, Supplementary Fig. 3e). Lastly, at 14 dpa and 28 dpa, we detected the expression of *tagln* and *cxcl12b*, which mark the smooth muscle cells localizing to the regenerating coronary arteries and the compact

Fig. 1 | A spatiotemporal transcriptomic and cellular transcriptomic atlas of the regenerating zebrafish heart. a Schematic diagram of the experimental design. Hearts were harvested pre-injury (i.e., uninjured), 6 hpa, 12 hpa, 1 dpa, 3 dpa, 7 dpa, 14 dpa, and 28 dpa and subjected to Stereo-seq (3 sections per heart, 6 hearts per stage, 8 stages; 105 total sections analyzed) or scRNA-seq (3 or 6 libraries per stage, 27 total libraries, 7656 cells on average per library). **b** Documentation of key cellular responses across sequential stages of regeneration. Spatial distributions of major cell-type domains in representative cardiac sections from Stereo-seq. **c** UMAP clusters discovered by scRNA-seq including all 8 time-points of zebrafish heart across sequential regeneration stages. Pie charts represent the proportions of cell types at each stage. Single asterisks show newly appearing cell types at different time points, and double asterisks show cell types with significantly higher proportions at 1 dpa and 3 dpa compared to the uninjured group. **d** Scaled cell-type compositions within each domain. The color legend is shared with (**b** and **c**). **e** Directed acyclic graph showing inferred cellular trajectories during the stages of zebrafish heart regeneration. Each row corresponds to one cluster annotation, and each column corresponds to one regenerative stage. Nodes and their colors denote cell-type or cell-state annotations. The gray lines represent lineage relationships between different cell types or states. Speculated nodes and their relationships are shown using dashed nodes and lines. **f**, **g** Organ-wide spatial visualization of imputed expression patterns of genes *cd63*, *hif1ab*, *acta1b*, and *mt-nd5* at the indicated regeneration stages. CM Cardiomyocyte, V Ventricle, A Atrium, comp. compact, activ. activation, dediff. dedifferentiation, prolif. proliferation, re-diff. re-differentiation, reg. pro-regenerative, BZm border zone myocardium, RZm remote zone myocardium, Vm Ventricular myocardium, Am Atrial myocardium, VAm Ventricular or Atrial myocardium, ECs Endothelial cells, SMC Smooth muscle cells, MC Macrophages, MFE Macrophages Fibroblasts and Endocardial cells, FB Fibroblasts, Epi Epicardium, RBC Red blood cells. Source data are provided as a Source Data file.

myocardium enriched domain, respectively (Fig. 1b, Supplementary Fig. 3d)[49–51]. Taken together, these data validate our atlas by accurately capturing multiple previously described transcriptional and cellular events spanning the entire regenerative window.

To investigate lineage relationships between cell types during zebrafish heart regeneration, we performed trajectory analysis on the populations discovered by scRNA-seq (Fig. 1e, Supplementary Data 4)[52]. Several cell types were consistently present during all stages without lineal connections to other populations (Fig. 1e). Other lineages were highly dynamic, giving rise to subpopulations appearing transiently in a stage-specific fashion, including activated endocardial cells (6 hpa to 1 dpa), proliferating macrophages (12 hpa to 1 dpa), pro-regenerative fibroblasts (3 dpa to 7 dpa), and subpopulation of dedifferentiated cardiomyocytes (12 hpa), consistent with their stage-specific roles within the broader context of heart regeneration (Fig. 1e).

Next, we sought to determine if those dynamic spatiotemporal gene expression patterns used to monitor cell-type behaviors during zebrafish heart regeneration are conserved in a mammalian model of heart regeneration. To that end, we evaluated homologous marker genes in a previously published spatial transcriptomic atlas of the regenerating neonatal mouse heart[53]. Numerous similarities were observed, including early injury-induced expression of *Aldh1a2* and *Pcna* as well as wound-specific expression of *Grn*, *Col12a1*, *Tagln*, and *Cxcl12* (Supplementary Fig. 4).

Previous studies have demonstrated that select genes, such as *aldh1a2*[21], become upregulated organ-wide following injury, only to become restricted to or enriched in specific locations thereafter. In our atlas, we discovered two additional genes exhibiting this behavior. Specifically, after global activation of *cd63* and *hif1ab* at 6 hpa, expression becomes preferentially localized to the wound edge by 1 dpa (Fig. 1f). Conversely, we observed organ-wide silencing of *acta1b* and *mt-nd5* on 6 hpa, followed by preferential re-expression at the wound edge between 7 dpa and 14 dpa (Fig. 1g). Accordingly, *acta1b* and *mt-nd5* were both expressed in atrial and ventricular cardiomyocyte cell clusters before the injury and then specifically in the border zone at 7 dpa and 14 dpa, respectively (Fig. 1g and Supplementary Data 2, 5). These results indicate that organ-wide activation or silencing of gene expression followed by spatial restriction is a broader phenomenon than previously appreciated.

Cellular dynamics of regenerating cardiomyocytes

Cardiac injury in regenerative hearts induces wound-edge CMs to undergo sequential phases of dedifferentiation, proliferation, and re-differentiation to regenerate amputated heart muscle[26,27,54]. To characterize these dynamic cell states at higher resolution, identify their transcriptional signatures, and discover potential regulators of cell-state transitions, we analyzed CM-related domains in our Stereo-seq dataset. In total, we discovered eight ventricular myocardium-enriched domains in uninjured and regenerating hearts that were annotated based on gene-expression profiles, including previously established markers (Supplementary Fig. 2b, Supplementary Fig. 5a–c, Supplementary Data 2). Five ventricular myocardium-enriched domains were injury-induced, localized to the wound edge, and stage-specific (Fig. 2a, Supplementary Fig. 2b, Supplementary Fig. 5a–c). They were annotated as BZ myocardium-enriched domains reflecting states of activation (activ.), dedifferentiation (dediff.), dedifferentiation-proliferation (dediff.-prolif.), proliferation (prolif.), and re-differentiation (re-diff.) of cardiomyocytes at 6 hpa, 12 hpa/1 dpa, 3 dpa, 7 dpa, and 14 dpa, respectively (Fig. 2a, Supplementary Fig. 2b, Supplementary Fig. 5a–c and Supplementary Data 2). They shared high correlations with each other (Supplementary Fig. 6a). Using cardiomyocytes (dediff.) as an example, we conducted cell-type deconvolution and confirmed cardiomyocytes (dediff.) enriched domain in the border zone at 12 hpa (Supplementary Fig. 6b). Furthermore, scRNA-seq trajectory analysis suggested the potential that the cardiomyocyte (dediff.) subtype in the wound border zone derived from ventricular cardiomyocytes (Fig. 1e)[26,27].

At 6 hpa, we observed the appearance of activated cardiomyocytes in BZm (activ.) along the wound edge (Fig. 2a and Supplementary Fig. 5a) characterized by the upregulation of several genes, including *tnfrsf11b*, *hspb6*, *hspb11*, *nppa* and *nppb* (Supplementary Fig. 5c and Supplementary Data 2). Gene set enrichment analysis identified "glycolysis and gluconeogenesis" as the top term for this BZm (activ.) domain (Supplementary Fig. 6c, d and Supplementary Data 6), consistent with metabolic switching of wound edge cardiomyocytes from oxidative phosphorylation to glycolysis[31,55]. At 12 hpa and 1 dpa, we detected dedifferentiated CMs along the wound edge based on high expression levels of *nppa* and *nppb* in BZm (dediff.) domain (Fig. 2a, Supplementary Fig. 5a–c and Supplementary Data 2). The *nppa* and *nppb* genes are expressed in the zebrafish myocardium during embryonic and larval stages[56,57]. During zebrafish heart regeneration, they were reported to become re-expressed in dedifferentiated CMs but not until 3 dpa[31,32]. In addition, the module score showed that many other heart development-related genes, including *hand2*, *tbx20*, *mustn1b*, *desma*, *mef2cb*, and *cacybp*, which have been reported in previous studies[22,31,32,43,58,59], were preferentially upregulated in the border zone starting from 12 hpa (Supplementary Fig. 5d), also hinting at a trend towards cellular dedifferentiation. Moreover, gene set enrichment analysis revealed that "glycolysis and gluconeogenesis" was also the top term for BZm (dediff.) (Supplementary Fig. 6c, d and Supplementary Data 6), indicative of ongoing glucose metabolism in wound edge cardiomyocytes. Together, these results suggest that CMs may adopt an activated state as early as 6 hpa and become dedifferentiating by 12 hpa.

To validate our Stereo-seq findings in vivo, we evaluated significant genes of the activated and dedifferentiated CM subpopulations in cardiac sections before and after injury by fluorescence in situ hybridization. The sections were co-immunostained with the MF20

https://doi.org/10.1038/s41467-025-59070-0

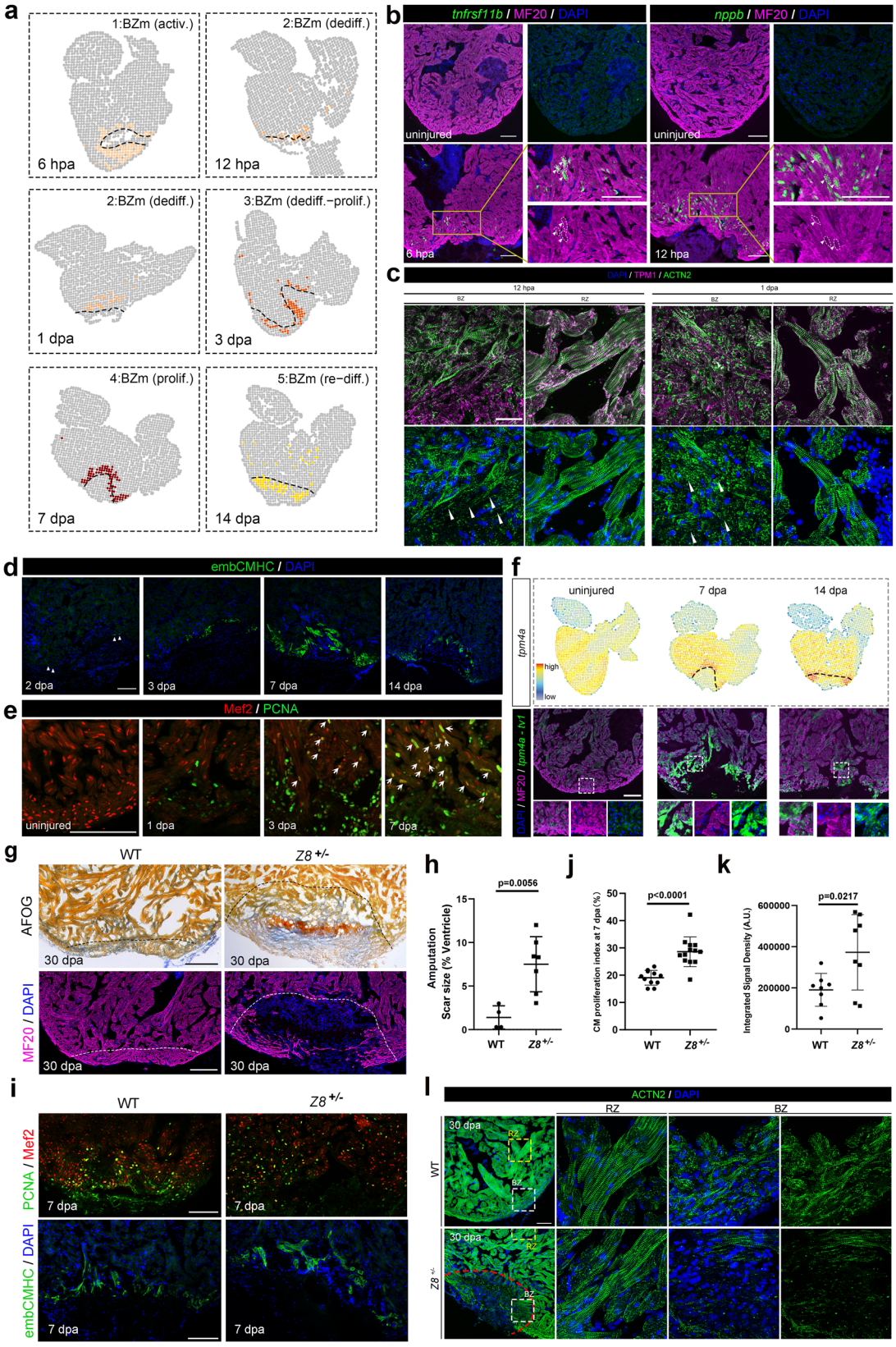

antibody to identify CMs. For visualizing activated CMs at 6 hpa, we chose the tumor necrosis factor (TNF) receptor gene *tnfrsf11b* because it was the most highly enriched gene in this subtype (Supplementary Fig. 5c and Supplementary Data 2). While uninjured hearts expressed little to no *tnfrsf11b*, injured hearts at 6 hpa expressed high *tnfrsf11b* levels in scattered CMs proximal to the wound edge (Fig. 2b). To visualize the distribution of dedifferentiated CMs, we relied on *nppb*, the top highly enriched gene in this subtype (Supplementary Fig. 5c and Supplementary Data 2). The *nppb* transcripts were undetectable before injury, becoming abundant specifically in CMs near the wound at 12 hpa (Fig. 2b, Supplementary Fig. 7c). To further verify the dedifferentiated states of CMs, we detected the state of sarcomeres at 12

Fig. 2 | Cellular dynamics of regenerating cardiomyocytes. a Spatially-resolved visualization of cardiomyocyte-related domains at different stages. **b** Representative images of uninjured or regenerating heart sections processed for fluorescence in situ hybridization to visualize the distributions of *tnfrsf11b* (green) and *nppb* (green). The sections were co-stained with the myocardial antibody MF20 (magenta) and counterstained with DAPI (blue). **c** Immunostaining of regenerating heart sections with antibodies against TPM1 (magenta), ACTN2 (green) and counterstained with DAPI (blue). **d** Immunostaining of regenerating heart sections with antibody against embCMHC (green) and counterstained with DAPI (blue). **e** Immunostaining images of uninjured or regenerating heart sections with antibodies against PCNA (green) or Mef2 (red). Arrows point to PCNA-positive CMs. **f** Spatial visualization of imputed expression of *tpm4a* at different stages (top). Representative images of uninjured or regenerating zebrafish heart sections processed for fluorescence in situ hybridization to visualize the distributions *tpm4a* (green) (bottom). The sections were co-stained with MF20 (magenta) and counterstained with DAPI (blue). **g** Representative images of cardiac sections from wild-type (WT) and $Z8^{+/-}$ hearts at 30 dpa stained with Acid Fuchsin-Orange G (AFOG) (top), or immunostained with MF20 (magenta) and DAPI (blue) (bottom). The dashed lines outline scar tissue. **h** Scatter plot showing scar area expressed as a percentage of ventricular area for WT and $Z8^{+/-}$ hearts at 30 dpa. **i** Representative immunostaining images of WT and $Z8^{+/-}$ zebrafish heart at 7 dpa stained with antibodies against PCNA (green) and Mef2 (red) (top) and immunostaining with embCMHC (green) and DAPI (blue) (bottom). **j** Scatter plot showing the CM proliferation index for WT and $Z8^{+/-}$ hearts at 7 dpa. **k** Scatter plot showing the fluorescence intensity of embCMHC in the ventricular area for WT and $Z8^{+/-}$ hearts at 7 dpa. **l** Representative images of cardiac sections from WT and $Z8^{+/-}$ hearts at 30 dpa. Immunostained with antibodies against ACTN2 (green) and counterstained with DAPI (blue). Scale bars: 100 μm for (**b, d**–**g, i** and **l**); 20 μm for (**c**). Source data are provided as a Source Data file.

hpa and 1 dpa. The results of immunofluorescence demonstrated that the Z-disk of sarcomeres near the wound disintegrated at 12 hpa, with more significant disintegration observed at 1 dpa (Fig. 2c), indicating that the CMs adopt a dedifferentiation state at 12 hpa. Surprisingly, the upregulation of these markers occurred at least 36 hours before the dedifferentiation marker embryonic cardiac myosin heavy chain (embCMHC)[60,61], which was barely detectable at 2 dpa, becoming stronger by 3 dpa, and peaking at 7 dpa (Fig. 2d). In addition to the model of apex resection, we detected the expression of *tnfrsf11b* in cryoinjured zebrafish hearts (Supplementary Fig. 7b). Fluorescence in situ hybridization results demonstrated that the expression of *tnfrsf11b* could be detected in CMs near the wound at 6 hours after cryoinjury, which was similar to the amputation injury model. Taken together, these data, including sarcomere breakdown, activations of injury-related, development-related, or glycolysis-related genes, supported that the dedifferentiation of CMs involves two CM cell-state transitions that occur much earlier than previously described[60,61].

At 3 dpa, we observed a subgroup of CMs in BZm (dediff.-prolif.) domain along the wound edge representing an intermediate cell state between dedifferentiated and proliferative CMs, characterized by simultaneous upregulation of *nppb, mustn1b, desma* and *pcna* (Fig. 2a; Supplementary Fig. 5a, c; Supplementary Fig. 7a and Supplementary Data 2). At 7 dpa, we documented a transition to proliferative CM cell state in BZm (prolif.) domain at the wound edge, based on increased expression of *pcna*, as well as strong induction of cell cycle regulators *cdk1*, *ccng1*, and *ccng2* (Fig. 2a, Supplementary Fig. 5a, c and Supplementary Data 2). PCNA protein expression is routinely used to detect proliferating CMs during heart regeneration studies in zebrafish[62]. It is crucial for promoting cell proliferation, facilitating DNA replication, and aiding in DNA repair processes[27]. By immunostaining, we validated that PCNA protein becomes detectable in wound edge CMs, beginning at 3 dpa and peaking at 7 dpa (Fig. 2e). To determine the specificity of the proliferating CMs gene signature, we analyzed the expression levels of the genes within this domain's top two gene set enrichment analysis terms, "striated muscle cell differentiation" and "regeneration" (Supplementary Fig. 6c), across all subpopulations. We learned that most of these genes were specific markers of BZm (prolif.) domain at 7 dpa (Supplementary Fig. 8c), indicative of a highly distinct molecular profile. For a subset of these marker genes (i.e., *acta1b*, *ccn1*, *spry4*, and *csrp3*), we validated their injury-induced localization to the wound edge at 7 dpa (Supplementary Fig. 7d). Among these genes, *ccn1* was reported to promote heart regeneration in neonatal mice[63].

Many signaling pathways are known to regulate CM proliferation[28,62,64–66]. To identify pathways that potentially regulate CM proliferation in a non-cell autonomous fashion due to signals emanating from surrounding non-cardiomyocyte lineages, we performed inter-cellular communication analysis using CellChat[67]. Our results uncovered the potential for crosstalk between the uninjured area and border zone of the myocardium through the JAM pathway at 3 dpa (Supplementary Fig. 8a and Supplementary Data 7). It also uncovered the potential for intercellular Notch signaling between multiple lineages, including CMs, endocardial cells, fibroblasts, and macrophages at 7 dpa (Supplementary Fig. 8b and Supplementary Data 7).

At 14 dpa, we identified the re-differentiated CM cell state in BZm (re-diff.) domain along the wound edge, exemplified by the upregulated expression of *cox6a2, cox5b2*, and *cox4i1l* (Fig. 2a, Supplementary Fig. 5a, c and Supplementary Data 2). The top gene set enrichment analysis term for this subtype was "oxidative phosphorylation", mirroring the top term for mature CM populations in the heart (Supplementary Fig. 6c and Supplementary Data 6), suggesting that by 14 dpa, regenerated CMs have adopted a relatively mature state. This was also reflected in a temporal expression analysis for genes comprising the "glycolysis and gluconeogenesis" or "oxidative phosphorylation" gene set enrichment analysis terms in regenerating border zone domains, which demonstrated that wound edge CMs predominantly rely on glucose metabolism soon after injury (i.e., 6 hpa - 1 dpa), returning to oxidative phosphorylation by 14 dpa (Supplementary Fig. 6d, e), consistent with previous reports[31,55]. The previous study in zebrafish hearts has confirmed that calcium handling is essential for CMs maturation[59]. Consistently, we observed the upregulation of Ca^{2+} handling-related genes at 14 dpa (Supplementary Fig. 6f), such as well-established EC coupling genes *atp2a2a* (*serca2*), *slc8a1a* (*ncx1*) and *ryr2b*[59,68–74]. Overall, the upregulation of oxidative phosphorylation and calcium-handling features associated with cardiac maturation were found in the late stage of regeneration.

The *tpm4a* gene is a potential regulator of CM re-differentiation during zebrafish heart regeneration

During our analysis, we noticed that *tpm4a* is highly expressed in proliferating and re-differentiated CMs in the border zone at 7 and 14 dpa, respectively, which we confirmed by immunostaining (Fig. 2f, Supplementary Fig. 7a, Supplementary Fig. 8c-e and Supplementary Data 2). The *tpm4a* has been reported to be required for maintaining the structural integrity of cardiac muscle fibers, thereby also modulating muscle contraction[75,76]. To investigate the role of the *tpm4a* in heart regeneration, we conducted functional studies with a previously reported *tpm4a* mutant line, *T2EGEZ8* (abbreviated *Z8*), a gene-trap insertion that creates a null allele[76]. Because *Z8* homozygotes die during larval stages, we performed amputation injuries on hearts from heterozygous adults (i.e., $Z8^{+/-}$ animals) and examined heart regeneration at 30 dpa. Remarkably, unlike wild-type (WT) animals, $Z8^{+/-}$ animals failed to replace the amputated myocardium with regenerated muscle, depositing significantly higher amounts of scar tissue (Fig. 2g, h). To exclude the possibility of delayed regeneration, we also analyzed heart regeneration in $Z8^{+/-}$ animals after cryoinjury. At 120 days post-cryoinjury (dpci), whereas WT animals successfully regenerated cryoinjured muscle, $Z8^{+/-}$ hearts failed to regenerate myocardium,

depositing significantly higher abundant scar tissue instead (Supplementary Fig. 8f, g), indicative of failed heart regeneration. Taken together, these data demonstrate that *tpm4a* is required for cardiac regeneration in zebrafish.

To explore the underlying mechanism, we performed immunostaining to quantify CM proliferation and dedifferentiation at 7 dpa. Unexpectedly, we discovered that CM proliferation (PCNA staining) was increased in $Z8^{+/-}$ hearts, and the degree of dedifferentiation (embCMHC staining) was higher than that in WT hearts at 7 dpa (Fig. 2i–k). The expression of embCMHC in $Z8^{+/-}$ hearts was comparable to that in WT hearts at 30 dpa (Supplementary Fig. 8h-i). Furthermore, immunostaining with ACTN2 revealed disorganized Z-disks of sarcomeres in BZ of $Z8^{+/-}$ hearts compared to WT animals at 30 dpa, indicating that the $Z8^{+/-}$ heart cannot properly assemble its sarcomeres at 30 dpa (Fig. 2l). Taken together, our results suggested that *tpm4a* may play a vital role during cardiac regeneration process, whereas *tpm4a* mutants failed to reorganize sarcomeres at the re-differentiation stage and consequently hampered heart regeneration.

Dynamic endocardial states in regenerating zebrafish hearts

As one of the earliest responses to cardiac injury, organ-wide activation of the endocardium serves multiple important functions, acting as a source of signaling molecules that stimulate CM proliferation, regulate remodeling of the extracellular matrix, and bolster coronary artery angiogenesis[21,45,62]. To achieve a deeper understanding of the dynamic cell states within the endocardium and their transcriptional signatures during zebrafish heart regeneration, we analyzed 65,593 total endocardial cells from across eight time points in our scRNA-seq dataset. We identified 5 endocardial subtypes that were annotated based on unique gene expression profiles, including previously established marker genes (Fig. 3a, b; Supplementary Fig. 9a, b and Supplementary Data 2). The subtypes included atrial, ventricular, *frizzled b*-positive (*frzb*+), activated, and proliferating endocardium, each with associated enrichment terms (Supplementary Fig. 10a). Whereas the atrial, ventricular, and *frzb*+ endocardial subtypes were detected at every time point, the activated and proliferative populations were observed transiently at specific regeneration stages (Figs. 1c, 3b and Supplementary Data 3). For instance, whereas activated endocardial cells were non-existent before injury, they composed about 19% and 14% of cardiac cells at 6 hpa and 12 hpa, respectively, falling to ~1% at 1 dpa, before disappearing thereafter (Fig. 3b and Supplementary Data 3). Interestingly, at 6 hpa and 12 hpa, sizeable proportions of ventricular endocardial cells, distinct from the activated subtype, were detectable, representing about 21% and 13.5% of cardiac cells, respectively (Fig. 3b and Supplementary Data 3), demonstrating that activation of the ventricular endocardium is more heterogeneous than previously recognized. The other regeneration-specific endocardial subtype, proliferating endocardium, was detectable in small percentages at 3 dpa (<1%) and 14 dpa (<1%) (Fig. 3b and Supplementary Data 3). We speculate that these cells were also present at 7 dpa (Fig. 1e), but given their low abundance, they likely fell below the level of detection at this stage. Deconvolution and mapping of the scRNA-seq data to the Stereo-seq slices revealed that activated endocardial cells were distributed organ-wide at 6 hpa, becoming preferentially localized to the wound edge at 12 hpa and 1 dpa (Fig. 3a, Supplementary Fig. 9c), consistent with previous reports[21].

Cell trajectory and RNA velocity analysis inferred that both activated and proliferating endocardial cells derive from ventricular endocardial cells (Fig. 1e, Supplementary Fig. 10c), consistent with cell state transitions from pre-existing endocardial cells[21]. At 1 dpa, some ventricular endocardial cells derive from the activated endocardial subtype (Fig. 1e), indicative of the reversible nature of the activated state.

Focusing more closely on the activated endocardial population, we identified markers that were highly specific to this subtype, including *aldh1a2*, *cd151*, *ackr3b*, *inhbaa* and *sema3aa* (Supplementary Fig. 10b and Supplementary Data 2). Accordingly, these genes were found to be induced organ-wide at 6 hpa, localizing preferentially to the wound starting from 12 hpa (Supplementary Fig. 3d, Supplementary Fig. 10d). Strong subtype-specific induction of these genes suggests that their molecular activities perform essential functions in the early endocardial response to injury.

Lastly, to discover potential intercellular interactions between cardiomyocytes and endocardial cells in the ventricle during early heart regeneration, we utilized CellChat to conduct a ligand-receptor analysis (Fig. 3c). At 6 hpa, 12 hpa and 1 dpa, we observed the potential for robust communication between endocardial cells (ventricular or activated) and cardiomyocytes (ventricular or dedifferentiated) mediated by the EPH, Notch, JAM, ncWNT, VEGF, and TGF-β signaling pathways (Fig. 3c and Supplementary Data 7). These predicted intercellular interactions provide the rationale for future explorations into possible crosstalk mechanisms between lineages, including subtypes.

Proliferative expansion of macrophages during early zebrafish heart regeneration

Next, we analyzed macrophages and their subtypes during zebrafish heart regeneration in our scRNA-seq dataset. We identified and annotated two macrophage subtypes, including non-proliferating macrophages (i.e., Macrophages) and injury-dependent proliferating macrophages [Macrophages (prolif.)] based on unique transcriptional signatures, including known marker genes (Fig. 3d; Supplementary Fig. 11a, b and Supplementary Data 2). Before injury, macrophages comprised about 7.6% of cardiac cells (Fig. 3d, Supplementary Fig. 11c, and Supplementary Data 3). During regeneration, this subtype was detected at every stage by scRNA-seq, peaking in abundance at ~32.8% of cardiac cells at 1 dpa (Supplementary Fig. 11c and Supplementary Data 3). Consistent with this early expansion of macrophages, we documented the transient appearance of proliferating macrophages, first at 12 hpa, and then in higher abundance at 1 dpa, when they localized predominantly to the wound (Fig. 3d, Supplementary Fig. 11c and Supplementary Data 3). Unexpectedly, we also documented macrophage enriched domain at 28 dpa preferentially in the outflow tract, an observation of unknown significance (Supplementary Fig. 1).

The top enrichment terms associated with proliferating macrophages encompassed all phases of the cell cycle, including DNA replication, mitosis, and cytokinesis (Supplementary Fig. 11d). Among the upregulated genes, those with the strongest induction were the proliferation marker gene *mki67*, along with cell division-related genes *smc2*, *smc4*, and *mad2l1* (Supplementary Fig. 11e), the latter of which are crucial for maintaining genomic stability, ensuring proper cell division, and facilitating tissue growth during regeneration.

We also found that macrophages with highly expressed *grnas* mainly appeared post cardiac injury (Supplementary Fig. 11b, f). The proliferating macrophage subtype was also marked by the immune-related genes *marco* and *grnas*, both of which were progressively enriched in the wound at 1 dpa (Supplementary Fig. 11b, f). We validated the injury-induced activation of *grnas* by fluorescence in situ hybridization on zebrafish hearts before and after injury. We observed upregulation of *grnas* close to the wound edge at 12 hpa and 1 dpa, and scattered in remote regions of the ventricle at 1 dpa (Fig. 3e and Supplementary Fig. 11f).

Through an analysis of cell lineage trajectories, we confirmed that proliferating macrophages derive from the general macrophage subtype (Fig. 1e). Collectively, our analysis identifies an early inflammatory response to cardiac injury characterized by proliferative expansion of macrophages in the wound, which peaks at 1 dpa. Because macrophages are immune cells responsible for phagocytosing cellular debris[77–79], their localized expansion within the

https://doi.org/10.1038/s41467-025-59070-0

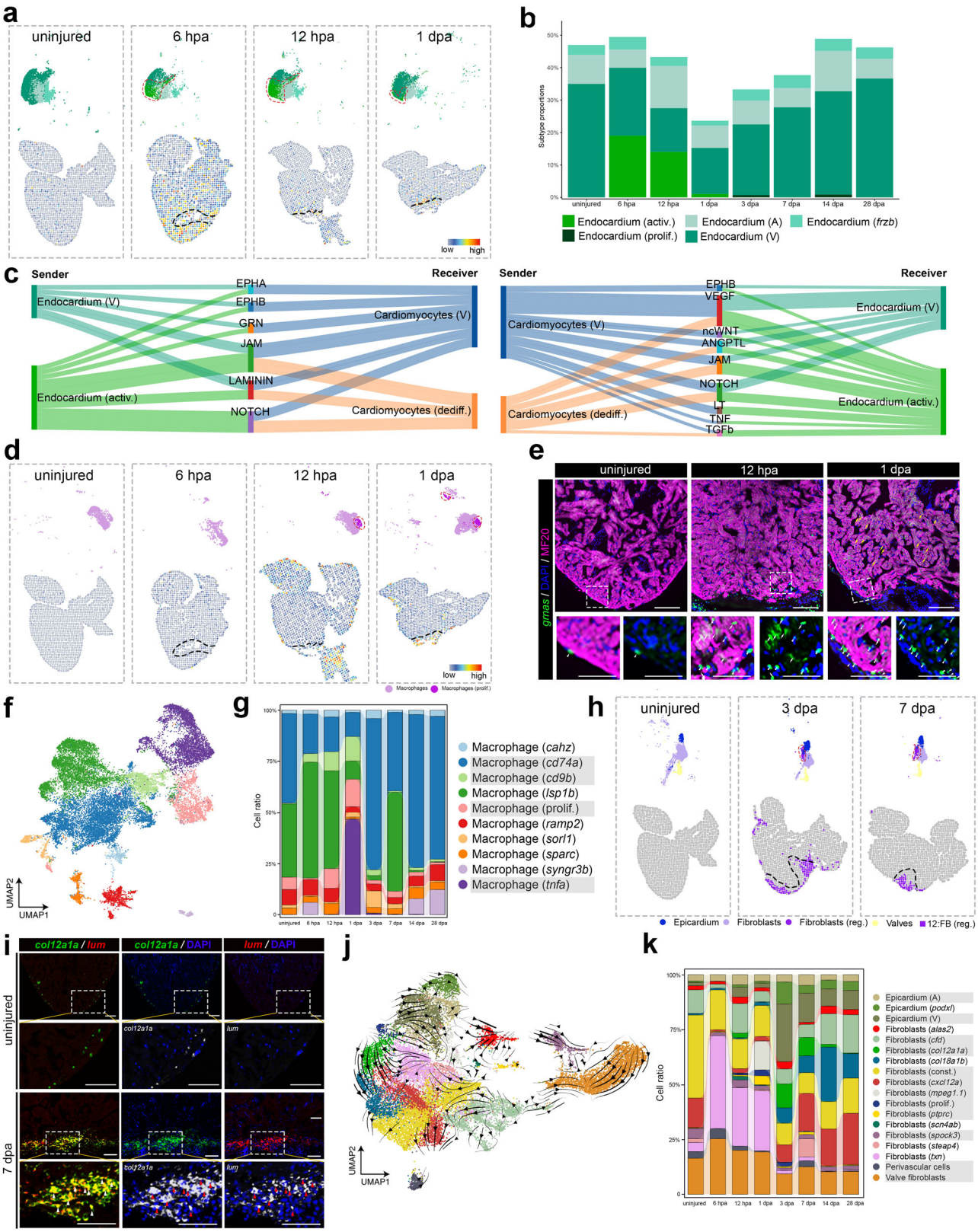

wound suggests that macrophage-mediated tissue clearance and remodeling are essential features of heart regeneration, consistent with previous reports[80]. To comprehensively investigate the dynamic composition of macrophages over time, we performed a more detailed analysis of all macrophage-related clusters and discovered significant diversity within this population, including ten distinct subtypes (Fig. 3f, g). We noticed that macrophages highly expressing *tnfa* appeared at 1 dpa, macrophages highly expressing *cd9b* were barely present in the uninjured heart, and *cd74a*-related cluster increased its abundance at 3 dpa, 14 dpa and 28 dpa compared to the early stage of regeneration (Fig. 3g). Notably, our time points were relatively more comprehensive compared to the previous study of Ma et al.[34], and we identified more subtypes, such as macrophages highly expressing *lsp1b*.

Fig. 3 | Dynamic endocardium, macrophage and fibroblast subtypes during zebrafish heart regeneration. a Dimensionality reduction of endocardium subtypes analyzed by scRNA-seq (top). Spatial visualization of Endocardium (activ.) abundance using cell type deconvolution. The color legend for the UMAP plots is shown in (**b**). **b** Bar graph showing the endocardial subtype percentages at each regeneration stage as determined by scRNA-seq (Red blood cells and Others were not included). **c** Sankey diagram showing the predicted pathways mediating cell-cell communications between cardiomyocytes and endocardium at 6 hpa, 12 hpa and 1 dpa. **d** Dimensionality reduction of macrophage subclasses determined by scRNA-seq (top) and spatial visualization of deconvoluted Macrophages (prolif.) abundance (bottom), respectively, at every regeneration stage. **e** Fluorescence in situ hybridization staining with *grnas* (green) and immunostaining with antibodies against MF20 (magenta) and DAPI (blue) in uninjured or regenerating hearts at 12 hpa or 1 dpa ($n = 4$ sections from 4 hearts for each time point). Arrows indicate cardiomyocytes, and arrowheads indicate non-cardiomyocytes. Scale bars: 100 µm for upper panels; 50 µm for lower panels. **f** UMAP clusters identified through scRNA-seq, including various subtypes of macrophages. The color legend for the UMAP plots is displayed in (**g**). **g** Bar graph showing the macrophage subtype percentages at each regeneration stage as determined by scRNA-seq. **h** Dimensionality reduction of fibroblast subpopulations analyzed by scRNA-seq (top) and spatial visualization domain 12: FB (reg.) by Stereo-seq (bottom), respectively, across all regeneration stages. **i** Fluorescence in situ hybridization staining with *col12a1a* (green), *lum* (red) and DAPI (blue) in uninjured or regenerating hearts at 7 dpa ($n = 4$ sections from 4 hearts for each time point). Arrowheads indicate co-located signals. Scale bars: 100 µm. **j** UMAP showing the subclusters and the RNA velocity of fibroblast as determined by scRNA-seq. The color legend for the UMAP plots is displayed in panel (**k**). **k** Bar graph showing the fibroblast subtype percentages at every regeneration stage as determined by scRNA-seq. Source data are provided as a Source Data file.

Investigation of the dynamic composition of the fibroblast during zebrafish heart regeneration

Fibroblasts perform essential roles in heart regeneration by synthesizing and secreting extracellular matrix components, which provide structural support and facilitate the remodeling of regenerating tissue[24,25,30,81]. To investigate the dynamic composition of the fibroblast population during zebrafish heart regeneration, we analyzed 21,172 fibroblast-related cells across the 8 time points in our scRNA-seq dataset (Supplementary Fig. 12a–d). We identified and annotated two predominant subtypes, including general fibroblasts (i.e., Fibroblasts) and pro-regenerative fibroblasts [i.e., Fibroblasts (reg.)] based on unique transcriptional signatures, including marker genes such as *col12a1a* and *col12a1b* as specific indicators of the pro-regenerative subtype (Supplementary Fig. 12c and Supplementary Data 2). As validation of our approach, identification of the pro-regenerative fibroblast subtype is consistent with a recent report[32]. Moreover, *col12* performs a critical function in ECM production during zebrafish heart regeneration, as previously documented[46,47]. The pro-regenerative fibroblasts were detected transiently at 3 and 7 dpa localized to the wound (Fig. 3h and Supplementary Fig. 12b), consistent with ongoing debris clearance and ECM remodeling.

As one reported source of cardiac fibroblasts[32], we also identified and analyzed epicardial cells (Fig. 3h; Supplementary Fig. 12a, d and Supplementary Data 2). At every stage, epicardial cells were ~3.6% or less of cellular content, except at 3 dpa, when the percentage rose to ~9% (Supplementary Fig. 12d and Supplementary Data 3), coincident with a highly activated and proliferative state[32,33]. Consistent with their known location, epicardial cells were accurately detected on the heart's surface at all stages (Supplementary Fig. 3b). We also identified valve fibroblasts and a small population of fibroblasts in which *mylkb* was highly expressed (Supplementary Fig. 12a, c).

To better understand the functional significance of the gene signatures associated with epicardial cells and fibroblast subtypes during regeneration, we performed gene set enrichment analysis (Supplementary Fig. 13a). For pro-regenerative fibroblasts, the top terms were related to ECM organization, ECM-cell interactions, cell adhesion, phagocytosis, and regulation of response to wounding (Supplementary Fig. 13a). All of these biological processes are instrumented for successful heart regeneration: ECM organization for structural support, cell migration and adhesion for tissue repair, cellular debris clearance for a healthy microenvironment, and modulation of the regenerative response for optimal healing. From this, we identified *lumican* (*lum*) upregulation in the top enrichment terms (Supplementary Fig. 13a and Supplementary Data 6). Specifically, *lum* expression was induced in pro-regenerative fibroblasts localized to the wound of the injured zebrafish heart at 3 dpa and 7 dpa (Supplementary Fig. 13b). We validated the injury-induced activation of *lum* in the wound by fluorescence in situ hybridization on zebrafish hearts before and after injury. We observed upregulation of *lum* transcript in a pattern that partially overlapped with the pro-regenerative fibroblast marker *col12a1a*, respectively, at 3 dpa or 7 dpa (Fig. 3i). To gain insights into cell-cell interactions, we conducted a ligand-receptor analysis using CellChat. At 3 dpa, we documented the potential for strong bidirectional communication between pro-regenerative fibroblasts and other cell types via COLLAGEN, MK, and FN1 signaling (Supplementary Fig. 13c and Supplementary Data 7).

Analysis of cell lineage trajectories inferred that pro-regenerative fibroblasts derive from epicardial cells (Fig. 1e), consistent with this well-documented epithelial-to-mesenchymal transition[32]. To further investigate the subtypes of fibroblast, we conducted a higher resolution unsupervised clustering, and 18 different subtypes of fibroblast were characterized (Fig. 3j, k and Supplementary Fig. 14a). The fibroblast subtypes identified in our study were well correlated with the previous study of Hu et al. (Supplementary Fig. 14b)[32]. Importantly, we identified more subtypes, such as fibroblasts (*txn*) at early stage of regeneration, fibroblasts (*steap4*) at 7 dpa, fibroblasts (*col18a1b*) at 14 dpa, epicardium (*podxl*), fibroblasts (*alas2*) and fibroblasts (*scn4ab*) (Fig. 3k). The RNA velocity analysis indicated that these subtypes might play a key role in the transitions of fibroblast cell states in zebrafish heart regeneration (Fig. 3j).

Comparative analysis reveals conserved transcriptional responses unique to highly regenerative hearts

The propensity of a heart to replace injured myocardium with fibroblast-derived scar tissue rather than new muscle defines non-regenerative and regenerative hearts[30]. In an attempt to identify transcriptional responses that are unique to regenerative hearts and conserved across species, we conducted a comparative analysis of regenerative and non-regenerative hearts (Fig. 4a, b and Supplementary Fig. 15a–c). Regenerative hearts included adult zebrafish and P1 (the day of birth) neonatal mice. Non-regenerative hearts included P8 (postnatal day 8) neonatal mice and adult human hearts before and after myocardial infarction. First, we identified 7 co-expression modules in zebrafish and generated a list of zebrafish genes within those module categories, all of which were highly related with heart regeneration of zebrafish (Supplementary Fig. 15a and Supplementary Data 2). We then determined the genes to which their homologs are induced following injury in regenerative and non-regenerative mammalian hearts based on previously published scRNA-seq[82] (Supplementary Fig. 15b, c). From this, we identified the upregulation of 29 genes as features of highly regenerative hearts, which show little to no induction in non-regenerative hearts (Fig. 4a, b). Specifically, we identified the increased expression of *atp6ap2* and *ifrd1* at 1 dpa and 6 hpa, respectively, which were localized to the wound of the injured zebrafish heart (Fig. 4c, d). Expressions of *Atp6ap2* and *Ifrd1* were also expanded in the regenerative P1 neonatal mouse heart at 1 day post myocardial infarction (dpMI) surgery when compared to sham-operated controls (Fig. 4b). By contrast, the expressions of *ATP6AP2* and *IFRD1* were relatively low in human hearts after myocardial infarction (Fig. 4b). These findings suggest that upregulation of the

https://doi.org/10.1038/s41467-025-59070-0

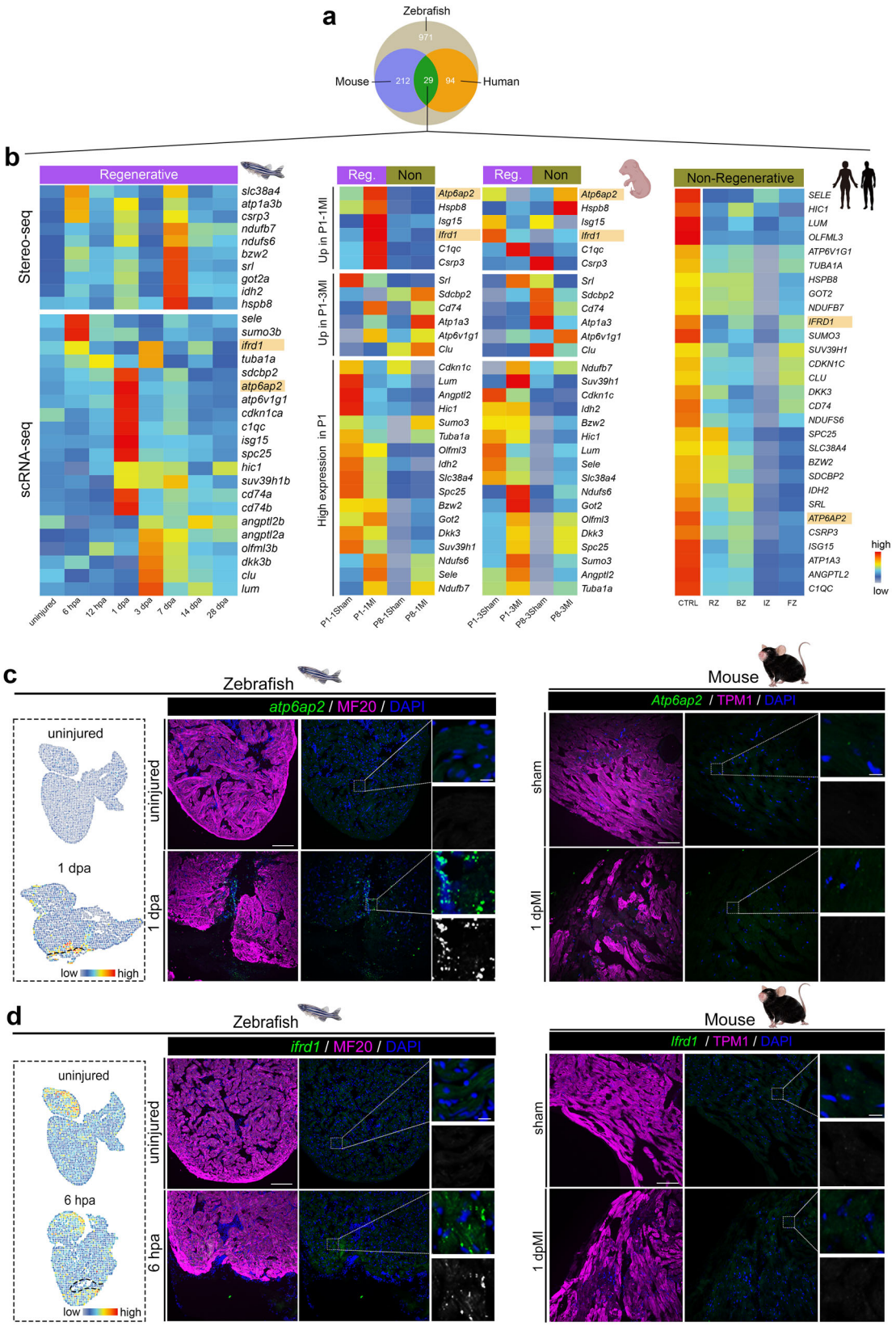

atp6ap2 and *ifrd1* might be an evolutionarily conserved feature of regenerative hearts.

We validated uninjured and the injury-induced activation of *atp6ap2* at 1 dpa and *ifrd1* at 6 hpa in the wound by fluorescence in situ hybridization on zebrafish. In contrast, we could not detect their expressions in adult mice hearts for sham controls and 1 day after MI surgery (Fig. 4c, d). Both genes were significantly upregulated in the wound of zebrafish but not expressed in non-regenerative hearts (Fig. 4c, d). These data demonstrate that our dataset provides opportunities to identify key factors associated with, and perhaps enabling, heart regeneration that are evolutionarily conserved across species.

Fig. 4 | Identification of conserved transcriptional responses shared by highly regenerative hearts. a Venn diagram illustrating genes that are upregulated or high expression in regenerative hearts (zebrafish and P1 mouse) and high expression in uninjured samples in non-regenerative hearts (P8 mouse and human). **b** Heatmaps showing the expression of overlapped genes selected in (**a**). **c** Spatial visualization of imputed expression of *atp6ap2* in uninjured and regenerating hearts at 1 dpa (left). Representative images of fluorescence in situ hybridization for *atp6ap2/Atp6ap2* (green) and immunostaining with antibodies against MF20 (magenta), TPM1(magenta) and DAPI (blue) on sections of zebrafish uninjured or regenerating hearts at 1 dpa and mouse hearts for sham surgery or 1 day after MI induces. Scale bars: 100 μm for left panels; 10 μm for right panels. **d** Spatial visualization of imputed expression of *ifrd1* in uninjured and regenerating hearts at 6 hpa, based on Stereo-seq data imputation using scRNA-seq data (left). Representative images of fluorescence in situ hybridization for *ifrd1/Ifrd1* (green) and immunostaining with antibodies against MF20 (magenta), TPM1(magenta) and DAPI (blue) on sections of zebrafish uninjured or regenerating hearts at 6 hpa and mouse hearts for sham surgery or 1 day after MI induces. Scale bars: 100 μm for left panels; 10 μm for right panels. MI, myocardial infarction; P1, the day of birth; P8, postnatal day 8; P1-1/3 (P8-1/3), collected at 1 or 3 days post-surgery; BZ, border zone; RZ, remote zone; IZ, ischaemic zone; FZ, fibrotic zone; CTRL, control. Source data are provided as a Source Data file.

Generation of a high-resolution organ-wide 3D transcriptomic and cellular atlas of the adult zebrafish heart

To overcome the limitations of inferring global spatial information from a small number of 2D slices per heart, we sought to create a high-resolution organ-wide 3D transcriptomic and cellular atlas of the adult zebrafish heart by integrating newly acquired Stereo-seq and scRNA-seq datasets (Fig. 5a). To that end, we meticulously sliced an entire adult heart into 167 consecutive sections and performed Stereo-seq. Based on inclusion criteria, we selected 119 high-quality sections for analysis, which encompassed a total of 100,846 individual spots with an average of 1055 unique molecular identifiers (UMIs) per spot (Supplementary Fig. 16 and Supplementary Data 1). We identified 12 unique spot identities that were annotated by major cell-type domains based on transcriptional signatures and well-established markers genes (Supplementary Fig. 16, Supplementary Fig. 17a and Supplementary Data 2). The 12 spot identities included one neuronal enriched domain which was not detected by our regeneration datasets, one valve domain, one smooth muscle cells enriched domain, one macrophage enriched domain, one epithelium enriched domain, one endothelium enriched domain, two red blood cells enriched domain, and four cardiomyocytes enriched domains. The Stereo-seq data were sufficient to perform 3D reconstructions (Supplementary Fig. 17b) of gene expression and domains, visualized in 3D models from any angle in our online interactive atlas (see below).

Nonetheless, to ensure that our spatial atlas contained a highly comprehensive representation of gene expression and cell types, we generated additional scRNA-seq data and integrated it with the Stereo-seq dataset. Specifically, we performed scRNA-seq separately on the three major anatomical structures of the zebrafish heart, including the ventricle, atrium, and BA, each pooled from 10 uninjured hearts (Fig. 5a). The data were combined into a single scRNA-seq dataset comprising 103,038 cells (Supplementary Data 1). After including scRNA-seq data from the uninjured time point in our regeneration study (Fig. 1c), the total number of cells increased to 158,939 (Supplementary Data 1). We identified and annotated 16 cell clusters based on unique transcriptional signatures and marker genes (Fig. 5b; Supplementary Fig. 18a, b and Supplementary Data 2). In contrast to the domains identified by Stereo-seq, we identified unique populations, including atrial and BA-specific endocardium, endothelial cells with coronary and lymphatic subtypes, fibroblasts, neutrophils, and T cells.

To integrate the scRNA-seq and Stereo-seq atlas, the gene expressions of Stereo-seq data were first imputed by scRNA-seq data, and then the spot identities of Stereo-seq data and scRNA-seq cell type mapping results were carefully merged. This integration allowed us to construct the first high-resolution organ-wide 3D transcriptional and cellular atlas of the adult zebrafish heart (Fig. 5c, Supplementary Fig. 19a, b and Supplementary Movie 1). In total, our integrated atlas contained spatial distributions of 18 cell types in the uninjured adult zebrafish heart. Users can query them through our online website (https://db.cngb.org/stomics/zebrafish_VRH/). As validation, we determined whether it accurately depicts the spatial distributions of previously characterized markers of unique cell types. Specifically, we queried the atlas for the spatial distributions of *myh7* and *myh6*, specific markers of ventricular and atrial cardiomyocytes, respectively[83], and retrieved their accurate chamber-specific expression patterns (Supplementary Fig. 20a–c). As further validation, we confirmed by fluorescence in situ hybridization that two predicted chamber-specific troponin genes, *tnni4a* and *tnnc1b*, exhibit ventricular and atrial-specific expression patterns, respectively (Supplementary Fig. 20a–d). Beyond cardiomyocytes, we relied on our atlas to determine that the *frzb*+ subpopulation of endocardial cells localizes to the BA (Fig. 5c, d), persuading us to re-annotate this cell type as “Endocardium (BA)”. We also confirmed by fluorescence in situ hybridization that a predicted potential marker of this subpopulation, *ccn1*, localizes specifically to the BA (Fig. 5e), providing further validation. Lastly, our integrated dataset allowed for an appreciation of the anatomic structures of regionalized tissues, such as valves, in the context of the entire heart (Supplementary Fig. 21a, b). Overall, our highly comprehensive atlas of the adult zebrafish heart allows for the accurate visualization of organ-wide gene expression, global cell-type distributions, and regionalized anatomic structures. It is also a testament to the reliability and robustness of integrating spatial transcriptomic and scRNA-seq datasets for delineating spatially-resolved biological information on an organ-wide scale.

Virtual 4D reconstruction of a regenerating zebrafish heart

Lastly, based on our spatial transcriptomic and scRNA-seq analysis of the regenerating zebrafish heart (Fig. 1a), we reconstructed a 4D “virtual regenerating heart” (VRH), encompassing both spatial information and time. It depicts the dynamic appearance of injury and stage-dependent major cell-type domains, including BZm (activ.) at 6 hpa, BZm (dediff.) at 12 hpa and 1 dpa, FB (reg.) at 3 dpa and 7 dpa, BZm (dediff.-prolif.) at 3 dpa, BZm (prolif.) at 7 dpa, and BZm (re-diff.) at 14 dpa (Fig. 5f, g and Supplementary Movie 2, 3). It also provides 4D expression patterns for all genes analyzed, including *tpm4a*, *col12a1a*, and *grnas*, which show dynamic expression patterns during heart regeneration (Supplementary Fig. 22). Lastly, to make our data widely accessible to the scientific community, we have established a public website (https://db.cngb.org/stomics/zebrafish_VRH/) containing both the high-resolution atlas of the uninjured heart and the VRH. This interactive database will provide researchers with a valuable resource for investigating the dynamic spatio-temporal behaviors of genes and cell types during zebrafish heart regeneration.

Discussion

We report the generation of a high-resolution, organ-wide, transcriptomic, and cellular atlas of the regenerating zebrafish heart in 3D space and time. Leveraging the strengths of Stereo-seq and scRNA-seq, our highly comprehensive atlas will serve as a valuable resource for investigators exploring the intricate mechanisms driving vertebrate cardiac regeneration. We reconstructed a 4-dimensional “virtual regenerating heart”, encompassing an unprecedented 569,896 cells or spots, sourced from 36 scRNA-seq libraries and 224 Stereo-seq slices.

https://doi.org/10.1038/s41467-025-59070-0

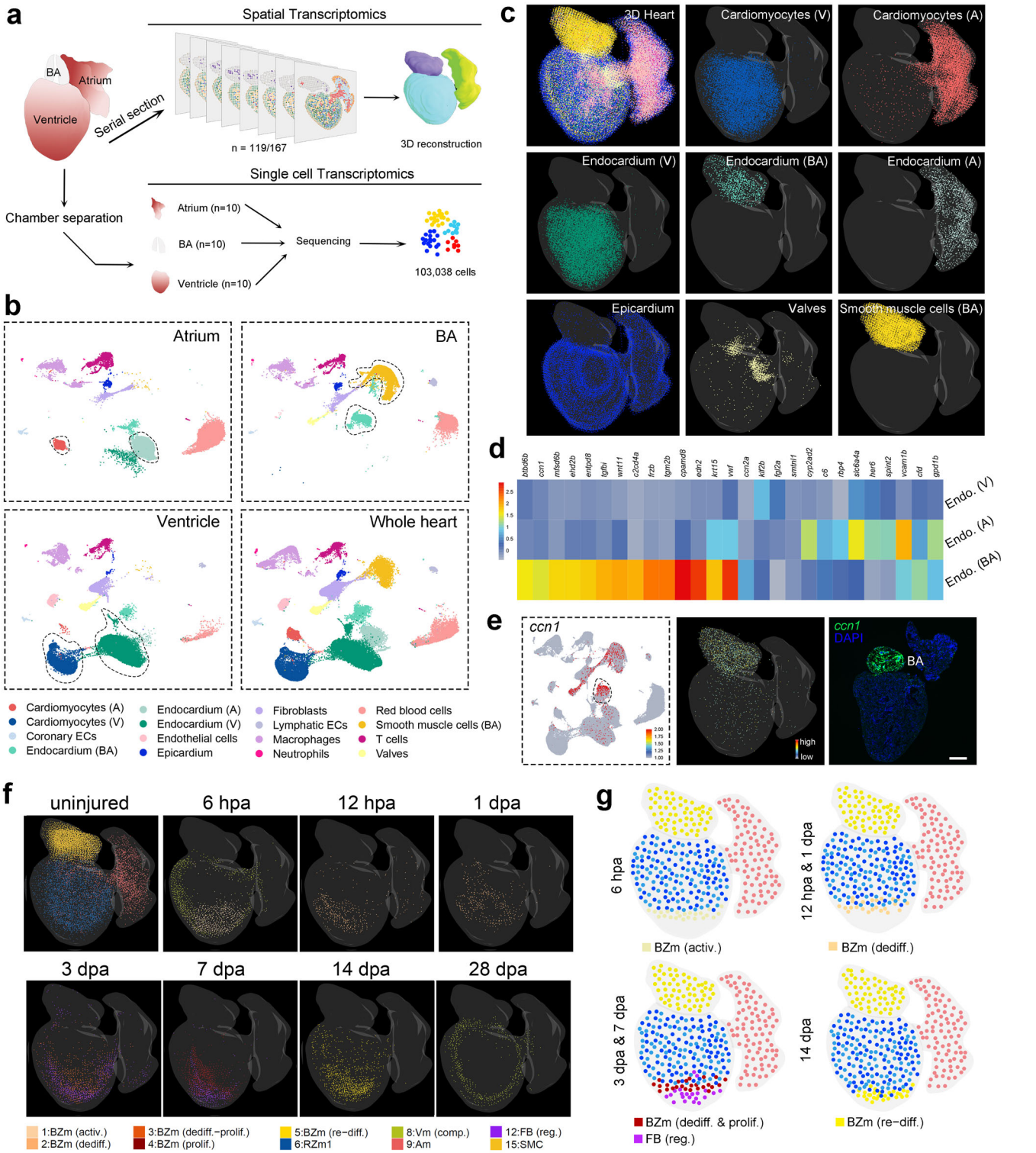

Fig. 5 | Generation of 3D and 4D spatiotemporal transcriptional and cellular atlases of the uninjured and regenerating zebrafish heart. a Workflow for reconstructing the 3D transcriptional landscape of the uninjured zebrafish heart. **b** UMAP plots of the scRNA-seq data from the uninjured atrium, ventricle, bulbus arteriosus (BA) and whole heart. The dashed lines identify major chamber-specific populations. **c** 2D projections of the 3D spatial distributions of major cell types in the uninjured zebrafish heart based on integrated data from Stereo-seq and scRNA-seq. **d** Heatmap showing the differential expression of genes highly expressed in the BA-specific endocardium subtype across all endocardial populations. **e** UMAP plot showing the expression of *ccn1* (left). 2D projection of the 3D spatial distribution of *ccn1* in uninjured zebrafish heart (middle). A representative image of a cardiac section processed for fluorescence in situ hybridization to detect *ccn1* (green), counterstained with DAPI (blue). Scale bar: 200 µm. **f** 2D projections of the 3D spatial distributions of dynamic cellular changes during zebrafish heart regeneration ($n = 15$ sections analyzed for uninjured; $n = 9–14$ sections analyzed per regenerative time point). **g** Graphical summary of key dynamic cellular changes during zebrafish heart regeneration. Source data are provided as a Source Data file.

These datasets were carefully sampled from 95 adult zebrafish hearts, spanning 8 distinct regenerative stages: pre-injury, 6 and 12 hpa, as well as 1, 3, 7, 14, and 28 dpa. The interactive VRH model is publicly accessible (https://db.cngb.org/stomics/zebrafish_VRH/), providing a virtual in situ perspective of the dynamic molecular and cellular processes underlying heart regeneration. Notably, our dataset provides comprehensive insights into the early stages of regeneration (6 hpa, 12 hpa, and 1 dpa), as well as whole-organ spatial coverage, thereby filling a significant gap in existing zebrafish heart regeneration datasets[32,34].

Using our highly comprehensive atlas, we characterized the dynamic changes in cell type composition and prevalence throughout heart regeneration. Specifically, we identified multiple injury-induced, regenerative cell types, including activated endocardium, proliferating macrophages, pro-regenerative fibroblasts, and regenerating CMs. The ability of pre-existing CMs to renter the cell cycle and generate new heart muscle through proliferative expansion has emerged as a primary determinant of successful heart regeneration[26,27,84]. It is widely recognized that CMs in the border zone undergo dedifferentiation and proliferation[27]. Through spatial clustering and cell type deconvolution analyses, we precisely traced the cellular prevalence and trajectories of proliferating CMs during regeneration, delineating 5 distinct clusters throughout space and time, spanning activation and re-differentiation. Although all of these clusters are related to the CM lineage, additional lineage tracing will be required to confirm their inter-relationships. More specifically, our findings indicate that regenerative CMs might become specified as early as 6 hpa, as evidenced by the activation of marker genes *tnfrsf11b* and *nppb*, suggesting that the myocardial regenerative process is active almost immediately after injury. One intriguing question is whether CMs of the regenerative P1 neonatal mouse heart also exhibit this early response, and whether it disappears as the mouse heart loses regenerative capacity, suggesting that it could be rate-limiting for heart regeneration. If so, focusing on how to induce the activation of CMs in non-regenerative hearts might be sufficient to stimulate cell cycle reentry and initiate the regenerative process. Interestingly, regarding spatial location, proliferating CMs are predominantly situated closer to the border zone edge at 7 dpa, whereas *tnfrsf11b*- and *nppb*-positive cells maintain a conspicuous distance from the wound at 6 hpa or 12 hpa. This phenomenon warrants further investigation to understand the functional significance of positional differences between these cell subtypes. Moreover, we implicated *tpm4a* may stimulate the re-differentiation of proliferating CMs, thereby promoting heart regeneration. While a previous study reported the existence of multiple transcript isoforms of *tpm4a*, which play varied roles in embryonic development[76], additional studies will be required to decipher isoform-specific functions of *tpm4a* in heart regeneration.

Despite investigations into the cardiac regenerative capacities of over twenty species in the past two decades, the common mechanisms underlying this process remain largely unknown[16]. Through comparative analysis of three species, we determined that regenerative hearts uniquely upregulate *atp6ap2* and *ifrd1* following injury, whereas non-regenerative hearts do not. This was observed specifically in regenerative zebrafish hearts, and we also speculate the observed upregulation of *Atp6ap2* and *Ifrd1* in regenerative neonatal mouse hearts. By contrast, non-regenerative hearts of P8 mice and humans did not show activation of *atp6ap2* and *ifrd1* homologous genes following mechanical or ischemic injury, respectively[38,82], which provides a strong rationale to investigate the role of *atp6ap2* and *ifrd1* in supporting natural heart regeneration. Since the adult human heart exhibits a cardiomyocyte turnover rate of approximately ~1% per year[85–87], identifying evolutionarily conserved features of regenerative hearts will likely pave the way for enhancing cardiomyocyte turnover and stimulating clinically impactful human heart regeneration in the wake of myocardial infarction.

In summary, the regenerative capabilities of the zebrafish heart are incompletely understood and are currently being extensively investigated. Our atlas and VRH will serve as a valuable resource for members of the cardiovascular and regeneration research communities. It will also serve as a foundation for integrating additional multi-omics datasets to further refine our appreciation of the transcriptional and cellular landscapes of heart regeneration. Ultimately, our publicly accessible resource holds considerable promise for aiding in elucidating the intricacies of vertebrate heart regeneration and advancing the discovery of potential therapies for treating human heart disease.

Methods

Experimental animals

This study was approved by the Ethics Committee of Ocean University of China. All protocols and procedures conformed with the *Guide for the Care and Use of Laboratory Animals* published by the US National Institutes of Health.

The zebrafish strains used in this study were wild-type AB, and adult fish aged between 6 to 12 months were used for all experiments[15]. A published strain, *T2EGEZ8*$^{+/-}$, was utilized[76]. The animal density was maintained at four fish per liter. The mice strain used in this study is C57BL/6J, and adult mice aged between 7 to 9 weeks were used for all experiments[88]. These mice were purchased from Jinan Pengyue Laboratory Animal Breeding Co., Ltd. Experimental mice were acclimated under controlled laboratory conditions for a minimum of 7 days prior to experimentation to minimize stress-induced variability. All mice were maintained in individually ventilated cages at a temperature of 22 ± 1 °C, humidity of 50 ± 10%, and a 12-hour light/dark cycle. All mice were given ad libitum access to food and water.

Heart injury

Zebrafish were anesthetized by immersion with 0.02% tricaine and immobilized in a dampened foam with the ventral side up. A little slit between the gills revealed the ventricle. For cardiac resection injury, insert forceps into the pericardial cavity with the left hand to grip the ventricular apex, then resect 20% of the ventricular apex, control bleeding with absorbent paper, and allow the heart to retract naturally. Close the incision with tweezers before transferring the fish to the recovery tank[15]. For cardiac resection injury, insert forceps into the pericardial cavity with the left hand to grip the ventricular apex, then resect 20% of the ventricular apex, control bleeding with absorbent paper, and allow the heart to retract naturally. Close the incision with tweezers before transferring the fish to the recovery tank[25,89]. Administer continuous gill irrigation via transfer pipette until autonomous swimming resumes. Maintain postoperative observation in the recovery tank for ≥5 minutes before transitioning to standard aquarium housing. The zebrafish were then euthanized with 0.04% tricaine, and the hearts were subjected to histology.

Myocardial infarction model in adult mice was established through ligation of the left anterior descending (LAD) coronary artery. Adult mice were anesthetized with isoflurane (3% isoflurane for induction, 1.5% isoflurane for maintenance). After the mice were fully anesthetized, they were placed on the operating table, intubated, and connected to a small-animal ventilator (RWD Life Science) that was used to assist the mice in breathing. Under fully-controlled ventilation, the chest area of the mice was shaved, make a 1-to-1.5 cm incision in the left thoracic region of the mouse, and incise through layers of skin and muscle sequentially to expose the ribs. Then, a thoracotomy was performed at the 3rd-4th intercostal space using surgical scissors to expose the heart, and a mouse rib spreader was applied to facilitate the exposure of the heart. The pericardium was carefully removed with forceps to clearly visualize the LAD coronary artery. The LAD was permanently ligated using a 6-0 silk suture at a position 2-3 mm from the left auricle. After ligation, the surgical site

was carefully examined for any signs of bleeding or oozing. The intercostal space and chest skin were closed with a 6-0 silk suture to ensure a tight seal without leakage. The tracheal tube was then removed, and the mice were placed on a heating pad (maintained at 37 °C) in a prone position to monitor their vital signs until they fully recovered. The sham operation group underwent all surgical procedures for MI except for the ligation of the coronary artery[88]. The mice were anesthetized using CO_2 and subsequently euthanized by cervical dislocation. Thereafter, the hearts were processed for histology.

Histological sectioning, staining, and imaging

For cryosectioning, hearts were dissected and fixed with 4% paraformaldehyde (PFA) in PBS overnight at 4 °C. After washing with PBS, the hearts were embedded in a 1.2% (wt/vol) agarose in 5% (wt/vol) sucrose-PBS solution, equilibrated in a 30% (wt/vol) sucrose-PBS solution overnight at 4 °C, and frozen for cryosectioning using a Leica cryostat (CM1860). 10 µm cryosections were used in all experiments[62].

Acid Fuchsin-Orange G (AFOG) staining labels heart muscles as orange and collagen as blue. For this staining, slides were hydrated in dH_2O at 25 °C, then incubated in Bouin's solution (Sigma # HT10132) for 2 hours at 60 °C and an additional hour at room temperature. Slides were rinsed with running water for 30 minutes, followed by incubation in 1% phosphomolybdic acid (solarbio #G3472) for 5 minutes and dH_2O for 5 minutes. The slides were then stained in an AFOG staining solution (1 g aniline blue [G-CLONE #CS2805], 2 g orange G [BBI #1936-15-8], and 3 g acid fuchsin [G-CLONE #CS3244] in 200 mL of dH_2O; pH 1.09) for 10 minutes, followed by rinsing with dH_2O and dehydration in 95% ethanol and 100% ethanol. Finally, the slides were placed in Xylene (BBI) twice for 2 minutes each and covered with Cytoseal coverslips (Thermo #8310-4)[64].

For immunofluorescence, cryosections were first immersed in boiling citric acid buffer (10 mmol/L) for 15 minutes for antigen retrieval, then continued to immerse until the buffer cooled to room temperature. After PBS washes, the sections were permeabilized with 0.5% Triton X-100 in PBS, and then blocked with a blocking buffer (5% BSA, 5% goat serum, 20 mmol/L $MgCl_2$) for 1 hour at room temperature. The cryosections were then incubated with primary antibodies in PBS containing 5% BSA overnight at 4 °C. Following this, secondary antibodies were added, and the sections were incubated at room temperature for 1 hour before being mounted with Neutral Balsam (Solarbio #G8590).

Primary antibodies used in this study include anti-embryonic cardiac myosin heavy chain (embCMHC, mouse, 1:50; DSHB); anti-myosin heavy chain monoclonal antibody (MF20, mouse, 1:50; DSHB), anti-Collagen, Type I pro-peptide (mouse, 1:50; DSHB), anti-PCNA (mouse, 1:200; Santa Cruz Biotechnology), anti-MEF2A + MEF2C (rabbit, 1:200; Abcam), anti-LUM (rabbit, 1:200; ABclonal), anti-ACTN2 (rabbit, 1:200; ABclonal), anti-TPM1 antibody (CH1, mouse, 1:200; DSHB). Secondary antibodies (1:200; Thermo Fisher Scientific) used in this study include Alexa Fluor 488 goat anti-mouse IgG (H + L), Alexa Fluor 568 goat anti-mouse IgG (H + L), Alexa Fluor 568 goat anti-rabbit IgG (H + L), and Alexa Fluor 488 goat anti-rabbit IgG (H + L).

Fluorescence in situ hybridization was performed to localize messenger RNAs (mRNAs) expressed during zebrafish heart and regeneration. To achieve this, Digoxygenin-labeled RNA and Fluorescein-labeled RNA probes were synthesized with TSA PLUS FLUORESCEIN (Akoyabio) according to the manufacturer's instructions. Fragments of these genes were cloned from a zebrafish heart cDNA library using oligos detailed in Supplementary Data 8.

AFOG staining images were captured using Nikon (DS-Ri2) and Zeiss ((Imager.Z2) microscopes. Immunofluorescence and fluorescence in situ hybridization images were captured using a Leica (DMi8) microscope.

Quantification analysis

Scar area in regenerated hearts was quantified at 30 dpa and 120 dpci. Fiji software was used to measure the total ventricular area as well as the scar area [fibrin (red) + collagen (blue)]. The scar area was normalized to the whole ventricular area to calculate the percentage of the scar size for each section[15,62]. Scar percentage data were gathered from at least 3 sections per heart and averaged to get each data point.

The cardiomyocyte proliferation index in regenerating hearts was quantified by manually counting $Mef2^+$ and $Mef2^+/PCNA^+$ cells in injury regions at 7 dpa indices using Fiji software with at least 3 sections per heart and averaged to get each data point.

Statistics and Reproducibility

Experimental statistical significance was tested using a two-tailed unpaired Student's *t* test, and *p* value was calculated using GraphPad Prism, unless stated otherwise. The graphs in Fig. 2h, j, k display the mean ± standard deviation (SD) of the compiled statistics, analyzed using a two-tailed unpaired Student's *t* test. All experiments in Fig. 2b, d, e, f used 4 hearts with 3 sections per heart at each time point. Figure 2c ($n = 4$) shows the results of one independent experiment. The experiments in Fig. 2g used WT hearts ($n = 4$) and $Z8^{+/-}$ hearts ($n = 7$), with a minimum of 3 sections analyzed for each heart. The experiments shown in Fig. 2h also employed WT hearts ($n = 4$) and $Z8^{+/-}$ hearts ($n = 7$). The experiments in Fig. 2i used WT hearts ($n = 3$) and $Z8^{+/-}$ hearts ($n = 5$), with at least 3 sections for each heart. The experiments in Fig. 2j used WT hearts ($n = 11$) and $Z8^{+/-}$ hearts ($n = 13$). The experiments in Fig. 2k used WT hearts ($n = 8$) and $Z8^{+/-}$ hearts ($n = 8$). The experiments in Fig. 2l used WT hearts ($n = 6$) and $Z8^{+/-}$ hearts ($n = 8$), with at least 3 sections for each heart. Figure 4c ($n = 4$) shows the results of one independent experiment; Fig. 4d ($n = 4$) shows the results of one independent experiment; Fig. 5e ($n = 4$) shows the results of one independent experiment.

Sample fixation and section preparation for Stereo-seq

Sample fixation was performed as the following steps. Briefly, fresh samples were rinsed in PBS and then the surface was wiped with clean gauze. The cleaned tissues were embedded with pre-cooled OCT and frozen with the dry ice, then transferred to a -80 °C refrigerator for storage before cryosection. The tissues were placed into a -20 °C freezing microtome for equilibration of 30 minutes before sectioning. Agilent 2100 bioanalyzer was used to assess the RNA quality of cryosections. Then, the pre-frozen cryosections of heart samples from healthy as well as injured zebrafish individuals were serially sectioned at 10 µm intervals throughout the entire heart in a Leica CM1950 cryostat. Each section was individually mounted onto the Stereo-seq chip with 3-minute incubation on a Thermocycler Adaptor at 37 °C, followed by methanol fixation at −20 °C for 40 minutes.

ssDNA staining and imaging of Stereo-seq sections

For tissue and cell visualization, sections on the chip were stained with a nucleic acid dye (Thermo Fisher, Q10212) for single-stranded DNA (ssDNA) prior to tissue permeabilization. ssDNA-stained sections were imaged using the Motic Custom PA53 FS6 microscope system and the images were stitched and processed using the PA53Scanner software platform.

Library construction and sequencing of Stereo-seq data

The Stereo-seq library construction and sequencing processes were conducted according to the corresponding protocols[90]. Briefly, sections were washed with 100 µL of 0.1× saline-sodium citrate buffer (SSC, Thermo, AM9770) supplemented with 0.05 U/µL RNase inhibitor (NEB, M0314L) to remove the staining solution. They were then permeabilized in 0.1% pepsin (Sigma, P7000, powder, ≥250 units/mg solid) in 0.01 M HCl buffer (pH = 2) and incubated at 37 °C for 12 minutes. High-resolution 1 × 1 cm Stereo-seq chips, which have DNA

nanoball (DNB) bins with 220 nm diameter and a center-to-center distance of 500 nm (regenerative samples) or 715 nm (3D samples), were used for in situ capture of RNA transcripts. And mRNAs were released and captured on the Stereo-seq chip, which was further reversely transcribed at 42 °C overnight using Superscript II [Invitrogen, 18064-014, 10 U/μL reverse transcriptase, 1 mM dNTPs, 1 M betaine solution PCR reagent, 7.5 mM $MgCl_2$, 5 mM DTT, 2 U/μL RNase inhibitor, 2.5 μM Stereo-seq-TSO (CTGCTGACGTACTGA-GAGGC/rG//rG//iXNA_G/) and 1 × First-Strand buffer] reverse transcription (RT) mix.

Furthermore, tissue sections were washed twice with 0.1 × SSC buffer and digested with tissue removal buffer (10 mM Tris-HCl, 25 mM EDTA, 100 mM NaCl, 0.5% SDS) at 37 °C for 30 minutes after in situ RT. The cDNA-containing chips were then subjected to Exonuclease I (NEB, M0293L) treatment for 1 hour at 37 °C and were finally washed once with 0.1× SSC buffer.

The remaining RT products were collected and amplified by KAPA HiFi Hotstart Ready Mix (Roche, KK2602) with 0.8 μM cDNA-PCR primer (CTGCTGACGTACTGAGAGGC). Sequencing libraries were prepared with PCR products undergoing the following steps: concentration quantification (Qubit™ dsDNA Assay Kit, Thermo, Q32854), DNA fragmentation (in-house Tn5 transposase at 55 °C for 10 minutes), PCR amplification (KAPA HiFi Hotstart Ready Mix (Roche, KK2602) with 0.3 μM Stereo-seq-Library-F primer (/5phos/CTGCTGACGTACTGAGAGG*C*A) and 0.3 μM Stereo-seq-Library-R primer (GAGACGTTCTCGACTCAGCAGA) and purification (Vazyme, N411-03). The purified PCR products were used to construct DNB libraries and sequenced on an MGI DNBSEQ-T1 sequencer (35 bp for read 1, 100 bp for read 2). Sequencing data were finally analyzed to derive a quantified spatial gene expression matrix at the subcellular scale.

Single-cell suspension preparation

The protocols for zebrafish heart dissociation and single-cell suspension isolation were prepared following the protocol described in Sander et al.[91]. The hearts of zebrafish were dissected throughout the regeneration stages and placed in pre-cooling Perfusion buffer (1× PBS, 10 mM HEPES [Sigma, #H3375], 30 mM taurine [Sigma, #T8691], 5.5 mM glucose [Sigma, #G7528], and 10 mM BDM [Sigma, #B0753]) on ice. Wash the blood in Perfusion buffer and then move the heart to a Digestion buffer (Perfusion buffer, 12.5 μM CaCl2, 2.5 mg/mL collagenase type II [Gibco, #17101-015] and 5 mg/mL collagenase type IV [Gibco, #17104-019]) to enzymatically digest the cell at room temperature about 2 hours in a shaker and gently flicked every 15 minutes to help with tissue disaggregation. Then digested cells go through a 70-μm cell strainer (BD) before centrifuged at 500 *g* for 10 minutes. Supernatant was removed, and the pelleted cells were then resuspended in PBS containing 0.04% BSA.

scRNA-seq library construction and sequencing

The DNBelab C4 was used for mRNA capturing. A total of six steps were applied to the single-cell suspensions to generate barcoded libraries: droplet generation, emulsion breakage, bead collection, reverse transcription, cDNA amplification, and purification. The cDNA production was sheared to 250-400 bps, and indexed sequencing libraries were constructed according to the manufacturer's protocol. Qubit ssDNA Assay Kit (Thermo Fisher Scientific) and Agilent Bioanalyzer 2100 were used for Qualification. DNBSEQ-T1 sequencer was used for further sequencing and generated reads containing 30 bp read 1 including the 10 bp cell barcode 1, 10 bp cell barcode 2 and 10 bp unique molecular identifier, 100 bp read 2 and 10 bp barcodes (sample index).

scRNA-seq data processing

The scRNA-seq data were processed following the DNBelab_C_Series_HT_scRNA-analysis-software (https://github.com/MGI-tech-bioinformatics/DNBelab_C_Series_HT_scRNA-analysis-software) pipeline, which include primary filtering, alignment, and gene expression generation. In brief, raw sequencing reads were filtered and quality-controlled using the in-house parseFqDev script. Then, the clean reads were aligned to the reference genome GRCz11, release 104 using STAR v2.7.2b[92] and annotated using Anno v1.4 in the pipeline. Finally, gene expressions of each cell were generated by PISA v0.12b[93] count tool.

scRNA-seq data clustering

The raw gene expressions of scRNA-seq were further processed by Seurat v4[94]. Cells with fewer than 200 genes and an average of more than ~24% mitochondrial genes were excluded. The filtered gene expression datasets for each time point were merged using the merge function and normalized by NormalizeData function. Then, the 2000 high variable features were identified by FindVariableFeatures and were used to do principal component analysis. The top 30 principal components were used for constructing the KNN network by FindNeighbors, and the cells were clustered by the FindClusters function with a resolution of 1.0 for each time point in the scRNA-seq regeneration dataset and 0.2 for the scRNA-seq chamber dataset.

Stereo-seq data processing

The reads were processed to generate gene expression GEM files. In brief, reads were aligned to the genome GRCz11, release 104 via STAR v2.7.2b[92]. Mapped reads with MAPQ > 10 were annotated and calculated by handleBam (https://github.com/BGIResearch/handleBam). UMIs with the same CID and the same gene locus were collapsed with 1 bp mismatch tolerated for possible sequencing and PCR errors. Reads overlapped more than 50% with the gene region were counted as transcripts.

For each slice, bin1 heatmap image was generated by Python script based on UMI counts and the ssDNA image was registered to heatmap image using TrakEM2 v1.3.6[95] as mask file. Out-of-tissue data were removed by GEM3D_toolkit (https://github.com/BGI-Qingdao/GEM3D_toolkit) gem_to_gemc command after manually refining the mask files. Samples in the same chip were separated by manually cutout mask image and GEM3D_toolkit mask_gem command and heart sections with unsatisfactory shapes were further filtered out. Gene expression matrices were divided into bins/spots with 50 × 50 DNB (bin50, ~35 μm diameter) for 3D Stereo-seq dataset, and 70 × 70 DNB (bin70, ~35 μm diameter) for the regeneration Stereo-seq dataset. These bin50/bin70 h5ad files were generated by GEM3D_toolkit gem_to_h5ad command and then converted to Seurat object by R script. All UMIs <100 bins were filtered out.

Stereo-seq data clustering

For the 3D atlas, 52 high-quality slices were selected by mean UMI > 1000. Scvi-tools v1.0.2[96] with all default parameters were used to remove batch effect, then the top 10 dimensions of scvi latent space were used to cluster by FindNeighbors and FindClusters functions (res = 1.2) of Seurat v4[94]. The labels from the 52 annotated high-quality slices were assigned to the remaining 67 medium-quality slices using RCTD v2.2.1[97].

The regeneration Stereo-seq data for each time point were further processed by Seurat v4[94] followed by SCTransform, merge, and RunPCA. Harmony v0.1.1[98] with the RunHarmony function was used to correct batch effects with PCA dimension reduction. Then, bins were clustered using FindNeighbors with top 30 harmony reductions, followed by FindClusters with a resolution parameter set at 1.4. To get more detailed major cell-type domain information, some mixed clusters were further processed to sub-clusters by Seurat and Harmony, followed by the same procedure described above but with lower resolution parameters 0.7.

Annotation

Clusters in scRNA-seq were annotated using known cell type-specific markers[31,32,34,83,99]. The cardiomyocytes (A) type was selected by *myh6*, and the cardiomyocytes (V) type was defined by *myh7*. Cardiomyocytes (dediff.) were annotated by *nppa*, *nppb*, and striated muscle cell differentiation genes in Supplementary Data 6. Endothelial cells were annotated by *cdh5* and *kdrl*, lymphatic ECs type was annotated by *lyve1a*, coronary ECs were annotated by *apln*, and coronary ECs (prolif.) were further separated by *pcna*. Endocardium was further selected by *spock3* and separated to endocardium (A) by *vcam1b*, endocardium (V) by *mb*, endocardium (activ.) by *aldh1a2*, endocardium (prolif.) by *pcna*, and endocardium (*frzb*) by *frzb*. Epicardium was defined by *gstm.3*, *wt1b*, *tbx18*, and *tcf21*. Fibroblasts were annotated by *dpt*, *dcn*, and *col1a2* and separated to fibroblasts (reg.) by *col12a1a* and *col11a1a*, fibroblast (SMC) by *mylkb*. Macrophages were annotated by *mfap4*, *mpeg1.1*, *grn1* and *grn2*, macrophages (prolif.) were further selected by *mki67*. Neutrophils were annotated by *mpx* and *lyz*. Proliferating cells were selected by *pcna*. Red blood cells were annotated by *cahz, hbba1*, *hbaa2*, and *hbaa1*. Smooth muscle cells were annotated by *myh11a*, *acta2*, and *rgs5a*. T cells were annotated by *il2rb*, *sla2*, and *ptprc*. Valves were annotated by *angptl7* and *abi3bpb*. In addition, we performed Pearson correlation analysis between our results and previous study[32] to refine the annotation, particularly for clusters that lacked significant expression of classical markers. All genes of scRNA-seq cell types identified by the Seurat FindAllMarkers function can be seen in Supplementary Data 2.

Based on the major cell-type markers, spatial locations, regeneration time points, as well as the results of the annotated cell types of scRNA-seq, Stereo-seq clusters were also annotated. These ventricular myocardium-enriched clusters near the injury area (border zone) were called BZm domains, in contrast, myocardium-enriched clusters located in the remote zone were called RZm domains. Specially, *mustn1b* and *desma*, which highly express in the embryonic cardiomyocytes, were upregulated in BZm compared to RZm. Besides, BZm (activ.) domain at 6 hpa was annotated by *tnfrsf11b*, *nppb*, *aldh1a2* and *cd63*; BZm (dediff.) domains at 12 hpa and 1 dpa were annotated by *nppb*, *aldh1a2* and *ctsd*; BZm (dediff.-prolif.) domain at 3 dpa was annotated by *nppb*, *pcna, myh7* and *col12a1a*; BZm (prolif.) domain at 7 dpa was annotated by *pcna, myh7, mb* and *col12a1a*; BZm (re-diff.) domain at 14 dpa was annotated by *cox6a2*, *cox5b2*, *cox4i1l*, *myh7* and *mb*. RZm1 and RZm2 (Vm1 and Vm2 in 3D) domains were annotated by *myh7*, *myl7*, *spock3* and *mb*. Vm (comp.) domain, which specially located in the outer layer of the ventricle, was annotated by *myh7* and *cxcl12b*. Am domain was annotated by *myh6* and *vcam1b*. MC domain was annotated by *mfap4, ctsd* and *grnas*. FB (reg.) domain was annotated by *col12a1a*. MFE domain was annotated by *marco*, *col12a1a*, and *aldh1a2*. Epi domain was annotated by *gstm.3*. SMC domain was annotated by *rgs5a*, *acta2*, and *myh11a*. Valves domain was annotated by *abi3bpb*. RBC domains were annotated by *cahz, hbaa2*, and *hbaa1* where RBC (A) also contained *myh6* and RBC (V) contained *myl7*. Endo (V) domain was annotated by *mb* and *cdh5*. Ner domain was annotated by *tuba1a* and *tuba1c*. Moreover, the Pearson correlations of clusters between different datasets and cell-type deconvolutions were conducted to refine the annotation results of domains, especially for clusters in which the expression of specific cell type markers are not significant. All genes of Stereo-seq domains identified by Seurat FindAllMarkers function can be found in Supplementary Data 2.

Deconvolution and mapping analysis

RCTD v2.2.1[97] was used to transfer labels of scRNA-seq reference dataset to each Stereo-seq slice. RCTD object of regeneration Stereo-seq was created with default settings. Then the run.RCTD function with the full model was used to generate the cell type deconvolution results. We next normalized the weights using normalize_weights function, then the estimated proportion of each cell type on each bin was calculated. To identify compositional differences between our data, we compared scRNA-seq cell type and Stereo-seq domain compositions following the guide of Kuppe et al.[38]. First, the median cell-type compositions in each heart were calculated, and then the median values were averaged across all hearts. Finally, the median-mean cell-type composition values were calculated within each domain.

Trajectory analysis

TOME[52] was used to generate lineage data. First, we integrated scRNA-seq data from adjacent time points using FindIntegrationAnchors and IntegrateData functions with default parameters, the lineage relationships were constructed by TOME, and weak links (edges weight <0.4) were filtered. The pair-wise correlation of cell types between each two adjacent time points was calculated using the scaled matrix of all gene expressions to assist in the manual refining of the final trajectory map.

RNA velocity analysis

Velocyto v0.17.17[100] was used to extract spliced and unspliced information from reads alignment bam files. Then the splice and unspliced datasets were used to estimate the RNA velocity. scVelo v0.3.1[101] was performed to calculate RNA velocity with a dynamical model.

Gene set enrichment analysis

Marker genes were detected using Seurat v4 with FindAllMarkers function. The top 100 differentially expressed genes based on fold change were further selected to do gene set enrichment analysis, and parameters pct.1 > pct.2 and p_val_adj < 0.01 were further applied in regeneration Stereo-seq data. Gene set enrichment analysis of each cluster was performed by online tools Metascape[102] with the D. rerio dataset as a reference.

Cell-cell communication analysis

CellChat v2.0.0[67] with "CellChatDB.zebrafish" database was used for both scRNA-seq and Stereo-seq's cell-cell communication analysis. We followed the tutorial protocol with default parameters, but used type = "truncatedMean" and trim = 0.1 in the computeCommunProb function. For Stereo-seq data, we used datatype = "spatial" in the createCellChat function.

Stereo-seq data imputation

For the regeneration of Stereo-seq data, Seurat v4[94] was used to perform gene imputation for each Stereo-seq slice using scRNA-seq data from the same time point, aiming to better visualize spatial gene expression patterns. For 3D Stereo-seq dataset, we first separated cells into three chambers by the mesh models using the MeshSub command of VT3D[103]. Then Seurat was used to impute Stereo-seq data of each chamber using corresponding scRNA-seq data. For both datasets, anchors were detected by CCA projection, and then genes were imputed by TransferData function. MAGIC v2.0.3[104] was applied to visualize *tpm4a* in Fig. 2f. Statistic calculations were not performed based on imputed data.

Cross-species analysis

The scRNA-seq data of regenerating hearts in neonatal mice[82] were downloaded from GEO under accession number GSE153481. Visium data of mouse regeneration hearts in neonatal mice[53] were downloaded from GEO under accession number GSE188888. The snRNA-seq data of human myocardial infarction[38] was downloaded from Zenodo (https://zenodo.org/record/6578047). All downloaded data were further processed by Seurat v4[94]. The gene expression was normalized by NormalizeData or SCTransform function.

Construction of 3D spatial distribution of cell types

Stereo-seq 3D dataset was first separated into three chambers by the mesh models using the MeshSub command of VT3D[103]. The RCTD analysis was performed by aligning the corresponding chamber's scRNA-seq data to the separated Stereo-seq data. To ensure the stability and reliability of the RCTD analysis, rare cell types were excluded from the reference scRNA-seq data. Moreover, unreasonable cell types, such as Endocardium (V) in the scRNA-seq data of atrial chamber, were also excluded. Only the cell in the "singlet" category and the two cells in the "doublet_certain" category were used to determine the spatial distribution of scRNA-seq cell types. A virtual bin close to the raw bin was created in the "doublet_certain" category. The final 3D atlas was manually integrated by considering the scRNA-seq distribution and the Stereo-seq distribution, selecting the clusters that displayed more reasonable spatial patterns.

Assignment of 3D coordinates

We used TrakEM2 v1.3.6[95] and the SEAM pipeline to semi-automatically align all 119 mask images of the 3D data into one uniform 3D coordinate system. All of those mask images were subsequently transformed to 3D mask images by 2D-to-3D affine matrix.

Following the scheme of brain map[105], we used an in-house Python script to fit 2D regeneration data into our 3D space. In brief, the mask images of regeneration Stereo-seq data were firstly matched to their closest 3D mask image based on shape similarity. Subsequently, 24 pairs of correspondence anchors for the 2D regeneration mask image and its closest 3D mask image were obtained. The warp transformation was calculated based on anchors to map the 2D coordinates into 3D space. After transformation, we discarded the out-mesh cells to achieve better visualization results.

Mesh model and online atlas website

Mesh models were built using Slicer (https://www.slicer.org) and our in-house Python scripts. We first created a 3D image where 1 pixel represents 10 μm and the gray value indicates the cell type at that position. Then, the Slicer Segmentation Editor was used to generate a raw mesh model based on the 3D image. The coordinate of the raw mesh model was then converted to unit 1 as 1 μm. A website was generated using VT3D[103] Atlas Browser functions for the online visualization of each dataset. To ensure optimal visualization of the 3D models, we recommend users to update their web browsers to the latest version and enable iframe support for a seamless interactive experience.

Reporting summary

Further information on research design is available in the Nature Portfolio Reporting Summary linked to this article.

Data availability

All raw data generated by Stereo-seq and scRNA-seq have been deposited in China National GeneBank DataBase (CNGBdb) Sequence Archive (CNSA) under accession code CNP0005245 and the NCBI database under accession number PRJNA1233465. Additional data, including processed data generated by Stereo-seq and scRNA-seq, associated analysis protocols, software and 3D models in this study can be accessed from the public website (https://db.cngb.org/stomics/zebrafish_VRH). The processed data are also available in the Zenodo repository under (https://zenodo.org/records/14991776). The published scRNA-seq data of regenerating hearts in neonatal mice used in this study are available in the GEO database under accession code GSE153481[82]. The published Visium data of mouse regeneration hearts used in this study are available in the GEO database under accession code GSE188888[53]. The published snRNA-seq data of human myocardial infarction are available in Zenodo (https://zenodo.org/record/6578047)[38]. The remaining data are available in the article, Supplementary Information or Source Data file. Source data are provided with this paper.

Code availability

The data analysis scripts are available to download from GitHub (https://github.com/BGI-Qingdao/ZebrafishHeartRegeneration_project) and Zenodo (https://zenodo.org/records/14991776).

References

1. Wang, Z., Ma, L., Liu, M., Fan, J. & Hu, S. Summary of the 2022 Report on Cardiovascular Health and Diseases in China. *Chin. Med. J. (Engl.)* **136**, 2899–2908 (2023).
2. Tsao, C. W. et al. Heart Disease and Stroke Statistics-2023 Update: A Report From the American Heart Association. *Circulation* **147**, e93–e621 (2023).
3. Prabhu, S. D. & Frangogiannis, N. G. The biological basis for cardiac repair after myocardial infarction: from inflammation to fibrosis. *Circ. Res.* **119**, 91–112 (2016).
4. Nguyen, P. D., de Bakker, D. E. M. & Bakkers, J. Cardiac regenerative capacity: an evolutionary afterthought? *Cell Mol. Life Sci.* **78**, 5107–5122 (2021).
5. Qi, Y. et al. Functional heart recovery in an adult mammal, the spiny mouse. *Int. J. Cardiol.* **338**, 196–203 (2021).
6. Peng, H. et al. Adult spiny mice (Acomys) exhibit endogenous cardiac recovery in response to myocardial infarction. *NPJ Regen. Med.* **6**, 74 (2021).
7. Nishiyama, C. et al. Prolonged myocardial regenerative capacity in neonatal Opossum. *Circulation* **146**, 125–139 (2022).
8. Haubner, B. J. et al. Complete cardiac regeneration in a mouse model of myocardial infarction. *Aging* **4**, 966–977 (2012).
9. Porrello, E. R. et al. Transient regenerative potential of the neonatal mouse heart. *Science* **331**, 1078–1080 (2011).
10. Zhu, W. et al. Regenerative potential of neonatal porcine hearts. *Circulation* **138**, 2809–2816 (2018).
11. Ye, L. et al. Early regenerative capacity in the porcine heart. *Circulation* **138**, 2798–2808 (2018).
12. Porrello, E. R. et al. Regulation of neonatal and adult mammalian heart regeneration by the miR-15 family. *Proc. Natl Acad. Sci. USA* **110**, 187–192 (2013).
13. Stockdale, W. T. et al. Heart Regeneration in the Mexican Cavefish. *Cell Rep.* **25**, 1997–2007.e1997 (2018).
14. Cano-Martínez, A. et al. Functional and structural regeneration in the axolotl heart (Ambystoma mexicanum) after partial ventricular amputation. *Arch. Cardiol. Mex.* **80**, 79–86 (2010).
15. Poss, K. D., Wilson, L. G. & Keating, M. T. Heart regeneration in zebrafish. *Science* **298**, 2188–2190 (2002).
16. Weinberger, M. & Riley, P. R. Animal models to study cardiac regeneration. *Nat. Rev. Cardiol.* **21**, 89–105 (2024).
17. Simões, F. C. & Riley, P. R. Immune cells in cardiac repair and regeneration. *Development* **149**, dev199906 (2022).
18. Simões, F. C. et al. Macrophages directly contribute collagen to scar formation during zebrafish heart regeneration and mouse heart repair. *Nat. Commun.* **11**, 600 (2020).
19. de Wit, L. et al. Cellular and molecular mechanism of cardiac regeneration: a comparison of newts, zebrafish, and mammals. *Biomolecules* **10**, 1204 (2020).
20. Lien, C. L., Schebesta, M., Makino, S., Weber, G. J. & Keating, M. T. Gene expression analysis of zebrafish heart regeneration. *PLoS Biol.* **4**, e260 (2006).
21. Kikuchi, K. et al. Retinoic acid production by endocardium and epicardium is an injury response essential for zebrafish heart regeneration. *Dev. Cell* **20**, 397–404 (2011).
22. Lepilina, A. et al. A dynamic epicardial injury response supports progenitor cell activity during zebrafish heart regeneration. *Cell* **127**, 607–619 (2006).

23. Kikuchi, K. & Poss, K. D. Cardiac regenerative capacity and mechanisms. *Annu. Rev. Cell Dev. Biol.* **28**, 719–741 (2012).
24. González-Rosa, J. M., Martín, V., Peralta, M., Torres, M. & Mercader, N. Extensive scar formation and regression during heart regeneration after cryoinjury in zebrafish. *Development* **138**, 1663–1674 (2011).
25. Chablais, F., Veit, J., Rainer, G. & Jaźwińska, A. The zebrafish heart regenerates after cryoinjury-induced myocardial infarction. *BMC Dev. Biol.* **11**, 21 (2011).
26. Kikuchi, K. et al. Primary contribution to zebrafish heart regeneration by gata4(+) cardiomyocytes. *Nature* **464**, 601–605 (2010).
27. Jopling, C. et al. JC. Zebrafish heart regeneration occurs by cardiomyocyte dedifferentiation and proliferation. *Nature* **464**, 606–609 (2010).
28. Marín-Juez, R. et al. Fast revascularization of the injured area is essential to support zebrafish heart regeneration. *Proc. Natl Acad. Sci. USA* **113**, 11237–11242 (2016).
29. Harrison, M. R. et al. Chemokine-guided angiogenesis directs coronary vasculature formation in zebrafish. *Dev. Cell* **33**, 442–454 (2015).
30. Sánchez-Iranzo, H. et al. Transient fibrosis resolves via fibroblast inactivation in the regenerating zebrafish heart. *Proc. Natl Acad. Sci. USA* **115**, 4188–4193 (2018).
31. Honkoop, H. et al. Single-cell analysis uncovers that metabolic reprogramming by ErbB2 signaling is essential for cardiomyocyte proliferation in the regenerating heart. *eLife* **8**, e50163 (2019).
32. Hu, B. et al. Origin and function of activated fibroblast states during zebrafish heart regeneration. *Nat. Genet.* **54**, 1227–1237 (2022).
33. Xia, Y. et al. Activation of a transient progenitor state in the epicardium is required for zebrafish heart regeneration. *Nat. Commun.* **13**, 7704 (2022).
34. Ma, H. et al. Functional coordination of non-myocytes plays a key role in adult zebrafish heart regeneration. *EMBO Rep.* **22**, e52901 (2021).
35. Farah, E. N. et al. Spatially organized cellular communities form the developing human heart. *Nature* **627**, 854–864 (2024).
36. Chen, A. et al. Single-cell spatial transcriptome reveals cell-type organization in the macaque cortex. *Cell* **186**, 3726–3743.e3724 (2023).
37. Wei, X. et al. Single-cell Stereo-seq reveals induced progenitor cells involved in axolotl brain regeneration. *Science* **377**, eabp9444 (2022).
38. Kuppe, C. et al. Spatial multi-omic map of human myocardial infarction. *Nature* **608**, 766–777 (2022).
39. Sampath Kumar, A. et al. Spatiotemporal transcriptomic maps of whole mouse embryos at the onset of organogenesis. *Nat. Genet.* **55**, 1176–1185 (2023).
40. Liu, C. et al. Spatiotemporal mapping of gene expression landscapes and developmental trajectories during zebrafish embryogenesis. *Dev. Cell* **57**, 1284–1298.e1285 (2022).
41. Kanemaru, K. et al. Spatially resolved multiomics of human cardiac niches. *Nature* **619**, 801–810 (2023).
42. Mantri, M. et al. Spatiotemporal single-cell RNA sequencing of developing chicken hearts identifies interplay between cellular differentiation and morphogenesis. *Nat. Commun.* **12**, 1771 (2021).
43. Wu, C. C. et al. Spatially resolved genome-wide transcriptional profiling identifies BMP signaling as essential regulator of zebrafish cardiomyocyte regeneration. *Dev. Cell* **36**, 36–49 (2016).
44. González-Rosa, J. M., Burns, C. E. & Burns, C. G. Zebrafish heart regeneration: 15 years of discoveries. *Regeneration* **4**, 105–123 (2017).
45. Lien, C. L., Harrison, M. R., Tuan, T. L. & Starnes, V. A. Heart repair and regeneration: recent insights from zebrafish studies. *Wound Repair Regen.* **20**, 638–646 (2012).
46. Wehner, D. et al. Wnt signaling controls pro-regenerative Collagen XII in functional spinal cord regeneration in zebrafish. *Nat. Commun.* **8**, 126 (2017).
47. Marro, J., Pfefferli, C., de Preux Charles, A. S., Bise, T. & Jaźwińska, A. Collagen XII contributes to epicardial and connective tissues in the zebrafish heart during ontogenesis and regeneration. *PLoS One* **11**, e0165497 (2016).
48. Kikuchi, K. Advances in understanding the mechanism of zebrafish heart regeneration. *Stem Cell Res.* **13**, 542–555 (2014).
49. Wu, T. et al. PRDM16 is a compact myocardium-enriched transcription factor required to maintain compact myocardial cardiomyocyte identity in left ventricle. *Circulation* **145**, 586–602 (2022).
50. Marín-Juez, R. et al. Coronary revascularization during heart regeneration is regulated by epicardial and endocardial cues and forms a scaffold for cardiomyocyte repopulation. *Dev. Cell* **51**, 503–515.e504 (2019).
51. Kim, J. et al. PDGF signaling is required for epicardial function and blood vessel formation in regenerating zebrafish hearts. *Proc. Natl Acad. Sci. USA* **107**, 17206–17210 (2010).
52. Qiu, C. et al. Systematic reconstruction of cellular trajectories across mouse embryogenesis. *Nat. Genet* **54**, 328–341 (2022).
53. Misra, A. et al. Characterizing neonatal heart maturation, regeneration, and scar resolution using spatial transcriptomics. *J. Cardiovasc. Dev. Dis.* **9**, 1 (2021).
54. Laube, F., Heister, M., Scholz, C., Borchardt, T. & Braun, T. Re-programming of newt cardiomyocytes is induced by tissue regeneration. *J. Cell Sci.* **119**, 4719–4729 (2006).
55. Fukuda, R. et al. Stimulation of glycolysis promotes cardiomyocyte proliferation after injury in adult zebrafish. *EMBO Rep.* **21**, e49752 (2020).
56. Man, J., Barnett, P. & Christoffels, V. M. Structure and function of the Nppa-Nppb cluster locus during heart development and disease. *Cell Mol. Life Sci.* **75**, 1435–1444 (2018).
57. Grassini, D. R. et al. Nppa and Nppb act redundantly during zebrafish cardiac development to confine AVC marker expression and reduce cardiac jelly volume. *Development* **145**, dev160739 (2018).
58. Hinits, Y. et al. Zebrafish Mef2ca and Mef2cb are essential for both first and second heart field cardiomyocyte differentiation. *Dev. Biol.* **369**, 199–210 (2012).
59. Nguyen, P. D. et al. Interplay between calcium and sarcomeres directs cardiomyocyte maturation during regeneration. *Science* **380**, 758–764 (2023).
60. Ben-Yair, R. et al. H3K27me3-mediated silencing of structural genes is required for zebrafish heart regeneration. *Development* **146**, dev178632 (2019).
61. Sallin, P., de Preux Charles, A. S., Duruz, V., Pfefferli, C. & Jaźwińska, A. A dual epimorphic and compensatory mode of heart regeneration in zebrafish. *Dev. Biol.* **399**, 27–40 (2015).
62. Zhao, L. et al. Notch signaling regulates cardiomyocyte proliferation during zebrafish heart regeneration. *Proc. Natl Acad. Sci. USA* **111**, 1403–1408 (2014).
63. Feng, T. et al. CCN1-induced cellular senescence promotes heart regeneration. *Circulation* **139**, 2495–2498 (2019).
64. Zhao, L., Ben-Yair, R., Burns, C. E. & Burns, C. G. Endocardial notch signaling promotes cardiomyocyte proliferation in the regenerating zebrafish heart through wnt pathway antagonism. *Cell Rep.* **26**, 546–554.e545 (2019).
65. Karra, R. et al. Vegfaa instructs cardiac muscle hyperplasia in adult zebrafish. *Proc. Natl Acad. Sci. USA* **115**, 8805–8810 (2018).
66. Gemberling, M., Karra, R., Dickson, A. L. & Poss, K. D. Nrg1 is an injury-induced cardiomyocyte mitogen for the endogenous heart regeneration program in zebrafish. *eLife* **4**, e05871 (2015).
67. Jin, S. et al. Inference and analysis of cell-cell communication using CellChat. *Nat. Commun.* **12**, 1088 (2021).

68. Kim, K. H., Kim, T. G., Micales, B. K., Lyons, G. E. & Lee, Y. Dynamic expression patterns of leucine-rich repeat containing protein 10 in the heart. *Dev. Dyn.* **236**, 2225–2234 (2007).
69. Fraysse, B. et al. Increased myofilament Ca2+ sensitivity and diastolic dysfunction as early consequences of Mybpc3 mutation in heterozygous knock-in mice. *J. Mol. Cell Cardiol.* **52**, 1299–1307 (2012).
70. Guo, A., Cala, S. E. & Song, L. S. Calsequestrin accumulation in rough endoplasmic reticulum promotes perinuclear Ca2+ release. *J. Biol. Chem.* **287**, 16670–16680 (2012).
71. Dewenter, M., von der Lieth, A., Katus, H. A. & Backs, J. Calcium signaling and transcriptional regulation in cardiomyocytes. *Circ. Res.* **121**, 1000–1020 (2017).
72. Eisner, D. A., Caldwell, J. L., Kistamás, K. & Trafford, A. W. Calcium and excitation-contraction coupling in the heart. *Circ. Res.* **121**, 181–195 (2017).
73. Sutanto, H. et al. Cardiomyocyte calcium handling in health and disease: Insights from in vitro and in silico studies. *Prog. Biophys. Mol. Biol.* **157**, 54–75 (2020).
74. Grote Beverborg, N. et al. Phospholamban antisense oligonucleotides improve cardiac function in murine cardiomyopathy. *Nat. Commun.* **12**, 5180 (2021).
75. Samson S. C. et al. 3-OST-7 regulates BMP-dependent cardiac contraction. *PLoS Biol* **11**, e1001727 (2013).
76. Zhao, L. et al. Heart-specific isoform of tropomyosin4 is essential for heartbeat in zebrafish embryos. *Cardiovasc. Res.* **80**, 200–208 (2008).
77. Yoo, W. et al. Progranulin attenuates liver fibrosis by downregulating the inflammatory response. *Cell Death Dis.* **10**, 758 (2019).
78. Tsuruma, K. et al. Granulin 1 promotes retinal regeneration in zebrafish. *Invest Ophthalmol. Vis. Sci.* **59**, 6057–6066 (2018).
79. Luo, W., Liu, S., Zhang, F., Zhao, L. & Su, Y. Metabolic strategy of macrophages under homeostasis or immune stress in Drosophila. *Mar. Life Sci. Technol.* **4**, 291–302 (2022).
80. Bevan, L. et al. Specific macrophage populations promote both cardiac scar deposition and subsequent resolution in adult zebrafish. *Cardiovasc Res.* **116**, 1357–1371 (2020).
81. Wang, J., Karra, R., Dickson, A. L. & Poss, K. D. Fibronectin is deposited by injury-activated epicardial cells and is necessary for zebrafish heart regeneration. *Dev. Biol.* **382**, 427–435 (2013).
82. Wang, Z. et al. Cell-type-specific gene regulatory networks underlying murine neonatal heart regeneration at single-cell resolution. *Cell Rep.* **33**, 108472 (2020).
83. Gafranek, J. T. et al. Sinus venosus adaptation models prolonged cardiovascular disease and reveals insights into evolutionary transitions of the vertebrate heart. *Nat. Commun.* **14**, 5509 (2023).
84. Senyo, S. E. et al. Mammalian heart renewal by pre-existing cardiomyocytes. *Nature* **493**, 433–436 (2013).
85. Lázár, E., Sadek, H. A. & Bergmann, O. Cardiomyocyte renewal in the human heart: insights from the fall-out. *Eur. heart J.* **38**, 2333–2342 (2017).
86. Bergmann, O. et al. Dynamics of cell generation and turnover in the human heart. *Cell* **161**, 1566–1575 (2015).
87. Bergmann, O. et al. Evidence for cardiomyocyte renewal in humans. *Science* **324**, 98–102 (2009).
88. Gao, F. et al. Reduced mitochondrial protein translation promotes cardiomyocyte proliferation and heart regeneration. *Circulation* **148**, 1887–1906 (2023).
89. González-Rosa, J. M. & Mercader, N. Cryoinjury as a myocardial infarction model for the study of cardiac regeneration in the zebrafish. *Nat. Protoc.* **7**, 782–788 (2012).
90. Chen, A. et al. Spatiotemporal transcriptomic atlas of mouse organogenesis using DNA nanoball-patterned arrays. *Cell* **185**, 1777–1792.e1721 (2022).
91. Sander, V., Suñe, G., Jopling, C., Morera, C. & Belmonte, Izpisua JC. Isolation and in vitro culture of primary cardiomyocytes from adult zebrafish hearts. *Nat. Protoc.* **8**, 800–809 (2013).
92. Dobin, A. et al. STAR: ultrafast universal RNA-seq aligner. *Bioinformatics* **29**, 15–21 (2013).
93. Shi, Q., Liu, S., Kristiansen, K. & Liu, L. The FASTQ+ format and PISA. *Bioinformatics* **38**, 4639–4642 (2022).
94. Hao, Y. et al. Integrated analysis of multimodal single-cell data. *Cell* **184**, 3573–3587.e3529 (2021).
95. Cardona, A. et al. TrakEM2 software for neural circuit reconstruction. *PLoS ONE* **7**, e38011 (2012).
96. Lopez, R., Regier, J., Cole, M. B., Jordan, M. I. & Yosef, N. Deep generative modeling for single-cell transcriptomics. *Nat. Methods* **15**, 1053–1058 (2018).
97. Cable, D. M. et al. Robust decomposition of cell type mixtures in spatial transcriptomics. *Nat. Biotechnol.* **40**, 517–526 (2022).
98. Korsunsky, I. et al. Fast, sensitive and accurate integration of single-cell data with Harmony. *Nat. Methods* **16**, 1289–1296 (2019).
99. Rubin, S. A. et al. Single-cell analyses reveal early thymic progenitors and pre-B cells in zebrafish. *J. Exp. Med.* **219**, e20220038 (2022).
100. La Manno, G. et al. RNA velocity of single cells. *Nature* **560**, 494–498 (2018).
101. Bergen, V., Lange, M., Peidli, S., Wolf, F. A. & Theis, F. J. Generalizing RNA velocity to transient cell states through dynamical modeling. *Nat. Biotechnol.* **38**, 1408–1414 (2020).
102. Zhou, Y. et al. Metascape provides a biologist-oriented resource for the analysis of systems-level datasets. *Nat. Commun.* **10**, 1523 (2019).
103. Guo, L. et al. VT3D: a visualization toolbox for 3D transcriptomic data. *J. Genet Genom.* **50**, 713–719 (2023).
104. van Dijk, D. et al. Recovering gene interactions from single-cell data using data diffusion. *Cell* **174**, 716–729.e727 (2018).
105. Fürth, D. et al. An interactive framework for whole-brain maps at cellular resolution. *Nat. Neurosci.* **21**, 139–149 (2018).

Acknowledgements

We thank Dr. Anming Meng (Tsinghua University) for sharing the T2EGEZ8 mutant line. We thank Dr. Jing-wei Xiong (Peking University) for extensive discussions and feedback. This work was financially supported by Laoshan Laboratory (LSKJ202203204), the National Natural Science Foundation of China (32170541 and 31970506 to LZ; 32170832 to YS), the Fundamental Research Funds for Central Universities, China (202012004 to LZ) and Guangdong Provincial Genomics Data Center (2021B1212100001 to TY). We acknowledge the support of the High-Performance Biological Supercomputing Center at the Ocean University of China for this research and China National GenBank (CNGB).

Author contributions

Conceptualization, L.Z., G.F., and Y.S.; investigation and experiments, M.L., Xuejiao Z., M.Z., J.G., F.Z., L.Y., X.L., S.P., Z.L., Y.C., X.S., N.Z., W.G., W.C., Y.Q., Z.Z., Y.Lu and J.W.; data curation, Xuejiao Z., M.L., L.L., L.G., T.Y., and J.C.; formal analysis, L.L., M.L., L.G., K.H., Xuejiao Z., M.X., Q.L., Y.Li, R.Z., and Xianghui Z.; writing – original draft, L.L., M.L., L.G., K.H., G.F., and L.Z.; writing – review & editing, L.Z., G.F., K.H., C.G.B., C.E.B., and Y.S.; visualization, M.L., and L.G.; supervision, L.Z., G.F., K.H., and Y.S.; project administration, L.Z., Y.S., and G.F.; funding acquisition, L.Z., G.F., Y.S., Y.G., H.Y., and X.X.

Competing interests

The authors declare no competing interests.

Additional information

Supplementary information The online version contains supplementary material available at https://doi.org/10.1038/s41467-025-59070-0.

Correspondence and requests for materials should be addressed to Kai Han, Long Zhao, Guangyi Fan or Ying Su.

Peer review information *Nature Communications* thanks Jan Philipp Junker and the other anonymous, reviewer(s) for their contribution to the peer review of this work. A peer review file is available.

[1]Qingdao Key Laboratory of Marine Genomics, BGI Research, Qingdao 266555, China. [2]State Key Laboratory of Genome and Multi-omics Technologies, BGI Research, Shenzhen 518083, China. [3]Key Laboratory of Evolution and Marine Biodiversity (Ministry of Education) and Institute of Evolution and Marine Biodiversity, Ocean University of China, Qingdao 266003, China. [4]College of Fisheries, Ocean University of China, Qingdao 266003, China. [5]College of Life Sciences, University of Chinese Academy of Sciences, Beijing 100049, China. [6]Department of Biology, University of Copenhagen, Copenhagen 2100, Denmark. [7]College of Marine Life Sciences, Ocean University of China, Qingdao 266003, China. [8]China National GeneBank, BGI Research, Shenzhen 518120, China. [9]MGI Tech, Shenzhen 518083, China. [10]BGI, Shenzhen 518083, China. [11]School of Basic Medicine, Qingdao University, Qingdao 266071, China. [12]Division of Basic and Translational Cardiovascular Research, Department of Cardiology, Boston Children's Hospital, Boston, MA 02115, USA. [13]Harvard Medical School, Boston, MA 02115, USA. [14]BGI Research, Sanya 572025, China. [15]BGI Research, Hangzhou 310030, China. [16]These authors contributed equally: Lei Li, Meina Lu, Lidong Guo, Xuejiao Zhang, Qun Liu, Meiling Zhang. ✉e-mail: hankai@genomics.cn; zhaolong@ouc.edu.cn; fanguangyi@genomics.cn; suying@ouc.edu.cn